



HAL
open science

Dissolution precipitation creep as a process for the strain localisation in mafic rocks

Amicia L Lee, Holger Stünitz, Mathieu Soret, Matheus Ariel Battisti

► To cite this version:

Amicia L Lee, Holger Stünitz, Mathieu Soret, Matheus Ariel Battisti. Dissolution precipitation creep as a process for the strain localisation in mafic rocks. *Journal of Structural Geology*, 2022, Accepted, pp.104505. 10.1016/j.jsg.2021.104505 . insu-03513841v1

HAL Id: insu-03513841

<https://insu.hal.science/insu-03513841v1>

Submitted on 6 Jan 2022 (v1), last revised 2 Nov 2022 (v2)

HAL is a multi-disciplinary open access archive for the deposit and dissemination of scientific research documents, whether they are published or not. The documents may come from teaching and research institutions in France or abroad, or from public or private research centers.

L'archive ouverte pluridisciplinaire **HAL**, est destinée au dépôt et à la diffusion de documents scientifiques de niveau recherche, publiés ou non, émanant des établissements d'enseignement et de recherche français ou étrangers, des laboratoires publics ou privés.

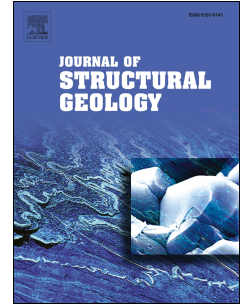


Distributed under a Creative Commons Attribution 4.0 International License

Journal Pre-proof

Dissolution precipitation creep as a process for the strain localisation in mafic rocks

Amicia L. Lee, Holger Stünitz, Mathieu Soret, Matheus Ariel Battisti



PII: S0191-8141(21)00229-7

DOI: <https://doi.org/10.1016/j.jsg.2021.104505>

Reference: SG 104505

To appear in: *Journal of Structural Geology*

Received Date: 6 August 2021

Revised Date: 22 December 2021

Accepted Date: 28 December 2021

Please cite this article as: Lee, A.L., Stünitz, H., Soret, M., Battisti, M.A., Dissolution precipitation creep as a process for the strain localisation in mafic rocks, *Journal of Structural Geology* (2022), doi: <https://doi.org/10.1016/j.jsg.2021.104505>.

This is a PDF file of an article that has undergone enhancements after acceptance, such as the addition of a cover page and metadata, and formatting for readability, but it is not yet the definitive version of record. This version will undergo additional copyediting, typesetting and review before it is published in its final form, but we are providing this version to give early visibility of the article. Please note that, during the production process, errors may be discovered which could affect the content, and all legal disclaimers that apply to the journal pertain.

© 2021 Published by Elsevier Ltd.

CRediT author statement

Amicia Lee: Conceptualization, Methodology, Formal analysis, Investigation, Visualization, Writing – Original Draft.

Holger Stünitz: Conceptualization, Resources, Writing- Review & Editing.

Mathieu Soret: Formal analysis, Investigation, Writing- Review & Editing.

Matheus Ariel Battisti: Formal analysis, Investigation, Writing- Review & Editing.

Journal Pre-proof

1 **Dissolution precipitation creep as a process for the strain localisation in mafic rocks**

2 Amicia L. Lee^{1*}, Holger Stünitz^{1,2}, Mathieu Soret², Matheus Ariel Battisti³

3 **amicia.lee@uit.no*

4 ¹*Department of Geosciences, UiT – Arctic University of Norway, Norway*

5 ²*Institut des Sciences de la Terre (ISTO), Université d'Orléans, France*

6 ³*Instituto de Geociências, Universidade Federal do Rio Grande do Sul, Brazil*

7

8 **Abstract**

9 The lower crust is, on average, mafic in composition and composed of minerals that remain
10 mechanically strong up to high temperatures. Here we show that dissolution-precipitation
11 creep (as a type of diffusion creep) plays a major role in deformation of gabbro bodies at upper
12 amphibolite facies conditions. The Kågen gabbro, N. Norway, is comprised of undeformed
13 gabbro lenses enclosed by mylonitised margins that deformed at 690 ± 25 °C and 1.0 to 1.1
14 GPa. The evolution of the microstructures and fabric of the low strain gabbro to high strain
15 margins were investigated. Original clinopyroxene and plagioclase dissolved during mineral
16 reactions and precipitated as new mineral phases: new plagioclase and clinopyroxene
17 (different compositions relative to the magmatic parents) and additional amphibole and
18 garnet. Microstructural and crystallographic preferred orientation (CPO) data indicate that
19 dissolution-precipitation creep is the dominant deformation mechanism. Amphibole shows a
20 strong CPO that is primarily controlled by orientated growth in the stretching direction. The
21 progression of mineral reactions and weakening is directly connected to a fluid-assisted
22 transformation process that facilitates diffusion creep deformation of strong minerals at far

23 lower stresses and temperatures than required by dislocation creep. Initially strong lithologies
24 can become weak, provided that reactions proceed during deformation.

25

26 **1. Introduction**

27 Strain localisation and fabric development in the lower continental and oceanic crust are
28 controlled by the active deformation mechanisms. The lower continental and oceanic crust
29 are, on average, mafic in composition and primarily composed of plagioclase, pyroxene and/or
30 amphibole (Rudnick & Fountain 1995), minerals that have been shown experimentally to
31 remain mechanically strong up to high temperatures (Mauler *et al.* 2000, Bystricky & Mackwell
32 2001, Rybacki & Dresen 2004, Moghadam *et al.* 2010). Understanding the mechanisms of such
33 deformation is the prerequisite to quantify the stresses, rates of deformation processes, and
34 to infer general conditions and environment of the tectonic setting of lower crustal rocks.

35 Viscous deformation in the crust occurs primarily by two mechanisms; (1) dislocation creep
36 and (2) diffusion creep combined with grain boundary sliding (GBS; e.g. Poirier 1985, Jessell
37 1987, Drury & Urai 1990, Wheeler 1992, Berger & Stünitz 1996). Dislocation creep involves
38 intracrystalline deformation, where dislocations move through the crystal structure by
39 processes of glide. Climb is required to minimise the internal strain energy resulting from
40 dislocation glide (Carter & Ave'Lallemant 1970, van Roermund & Lardeaux 1991, Platt & Behr
41 2011). The process of diffusion creep is the result of solid-state diffusion of atoms (diffusive
42 mass transfer) through a crystal lattice, termed Nabarro-Herring creep, or along grain
43 boundaries, termed Coble creep (Poirier 1985, Wheeler 1992, Langdon 2006). If diffusion is
44 combined with dissolution in and precipitation from an aqueous fluid, pressure solution allows
45 material to be transported along grain boundaries in a fluid film rather than the movement of

46 atoms and vacancies (Rutter 1983). Coble creep and pressure solution are efficient processes
47 at lower temperatures than Nabarro-Herring creep and are far more likely to be dominant in
48 crustal materials (Elliott 1973, Poirier 1985). Dissolution-precipitation creep (DPC) is a term
49 generally used for the process of dissolving and precipitating material during diffusion creep.
50 DPC can occur within a single phase or it may be accompanied by metamorphic reactions. In
51 the latter case the material is precipitated as new phase(s), resulting in transformation
52 weakening (Stünitz 1993, Okudaira *et al.* 2015, Marti *et al.* 2017, Stünitz *et al.* 2020, Mansard
53 *et al.* 2020a).

54 Amphibole and plagioclase are common mid to lower crustal minerals and as a consequence
55 they are considered to play a large role in controlling the strength of crustal scale structures
56 (Rudnick & Fountain 1995, Tatham *et al.* 2008, Lloyd *et al.* 2011). The strength and active
57 deformation mechanisms of plagioclase at mid to lower crustal conditions have been the
58 subject of many studies (e.g. Marshall & McLaren 1977, Tullis 1983, Dimanov *et al.* 1999, Kruse
59 *et al.* 2001, H. Stünitz *et al.* 2003, Rybacki & Dresen 2004, Terry & Heidelbach 2006, Miranda
60 *et al.* 2016), yet the rheology of mafic minerals have received little attention so far (Bystricky
61 & Mackwell 2001, Dimanov *et al.* 2003, 2011, Dimanov & Dresen 2005, Moghadam *et al.*
62 2010), and that of amphibole remains poorly understood.

63 Experimentally, amphibole is considered to be strong at lower crustal conditions (Brodie and
64 Rutter, 1985; Shelley, 1994), and only exhibits weakening with mechanical twinning and
65 dislocation glide at high stresses and strain rates (Rooney *et al.* 1970, 1975, Dollinger & Blacic
66 1975, Morrison-Smith 1976, Hacker & Christie 1990). Amphibole exhibits a fabric during
67 diffusion creep and reaction (Getsinger and Hirth 2014). Naturally deformed amphiboles have
68 been shown to display brittle deformation at greenschist to amphibolite facies conditions

69 (Allison & La Tour 1977, Brodie & Rutter 1985, Nyman *et al.* 1992, Stünitz 1993, Babaie & La
70 Tour 1994, Imon *et al.* 2004, Soret *et al.* 2019). Evidence for crystal plasticity has been
71 interpreted (often based upon CPO) in natural samples at temperatures from 450 to >650°C
72 via dynamic recrystallization, dislocation creep on (100)[001] and subgrain formation by
73 dislocation glide (Biermann & van Roermund 1983, Cumbest *et al.* 1989, Skrotzki 1992,
74 Siegesmund *et al.* 1994, Díaz Aspiroz *et al.* 2007, Pearce *et al.* 2011). Additionally, evidence
75 for diffusion creep of natural amphibole has been inferred by dissolution-precipitation creep
76 and/or diffusion-accommodated GBS forming strong fabrics at upper greenschist to upper
77 amphibolite facies conditions (Berger & Stünitz 1996, Imon *et al.* 2002, 2004, Okudaira *et al.*
78 2015, Giuntoli *et al.* 2018, Soret *et al.* 2019, Graziani *et al.* 2020, Mansard *et al.* 2020a, 2020b).
79 Naturally deformed amphibole usually produces strong fabrics and is thought to be
80 responsible for the strongly anisotropic lower crust (Mainprice & Nicolas 1989, Tatham *et al.*
81 2008, Lloyd *et al.* 2011, Ji *et al.* 2013).

82 From the short summary of literature results above, it emerges that the relationships between
83 chemical reactions, fabric formation, and deformation mechanisms in mafic rocks are poorly
84 understood, yet they play a major role for understanding the mechanical strength of the crust
85 and for localizing deformation in different tectonic settings. In this study, we analyse the
86 microstructures and chemistry of the deformed margin of the Kågen gabbro (N. Norwegian
87 Caledonides) to show the influence of mineral reactions and fluids on active deformation
88 mechanisms and strain localisation during deformation at amphibolite facies conditions.

89

90 **2. Geological setting**

91 The Caledonides formed from convergence and collision of Baltica and Laurentia during the
92 Silurian to Devonian periods. In northern Norway, large-scale nappe stacking preserves a
93 section of autochthonous Baltica basement and ophiolites with varying metamorphic grades
94 and deformation style (Corfu *et al.* 2014). The Reisa Nappe Complex (from bottom to top:
95 Vaddas, Kåfjord, and Nordmannvik nappes; Figure 1a) in northern Troms is considered to be
96 lapetus-derived or part of the outer Baltica margin (Andersen *et al.* 1982, Corfu *et al.* 2006). It
97 underwent viscous deformation and metamorphism at amphibolite- to granulite-facies
98 conditions with pervasive partial melting (Roberts & Sturt 1980, Faber *et al.* 2019).

99 The Kågen gabbro intruded into amphibolite to granulite-grade metasediments of the Vaddas
100 Nappe and is exposed on the islands of Kågen and Arnøya (Figure 1b). The emplacement of
101 the gabbro occurred at 439 ± 1 Ma (U-Pb zircon concordia age; Faber *et al.* 2019), and cooling
102 is recorded over a broad temperature range of 650-900°C at pressures of 0.7-0.9 GPa that
103 correspond to depths of 26-34 km resulting in partial melting of the adjacent felsic and
104 metapelitic rocks (Getsinger *et al.* 2013, Gasser *et al.* 2015, Faber *et al.* 2019). A mantle melt
105 source and extensional setting is implied from the tholeiitic composition of the gabbro in the
106 Vaddas Nappe (Lindahl *et al.* 2005).

107 The sample location is situated near the western margin of the Kågen gabbro on Arnøya (GR:
108 70.04389N, 20.71444E). The outcrop region consists of undeformed gabbro lenses with
109 mylonitised margins enveloping the lenses (Figure 2a), and is approximately 0.7 km west of
110 samples studied by Getsinger *et al.* (2013). The area studied by Getsinger *et al.* (2013) hosts
111 several hydrous pegmatite intrusions that locally hydrated the gabbro and partitioned
112 deformation during emplacement of the gabbro. The deformed margins of gabbro pods in our
113 sample area are not associated with pegmatite intrusions, and, together with the formation

114 of a regional fabric close to margin of the gabbro body, indicate a different setting for the
115 deformation.

116 The Vaddas Nappe underwent shearing at 432 ± 6 Ma (TIMS, mean $^{206}\text{Pb}/^{238}\text{U}$ age in titanite),
117 temperatures of 630-640°C, pressures of 1.2-1.3 GPa and depths 43-46 km during the main
118 Scandian collision event of the Caledonides (Faber *et al.* 2019), and the gabbro outcrops of
119 this study have been deformed during this orogenic stage. This paper investigates the
120 processes occurring during deformation of mafic rocks and where the observed deformation
121 in the Kågen gabbro is related to the Vaddas Nappe and Caledonian deformation history.

122

123 **3. Methods of study**

124 In this paper we analysed polished thin sections in order to investigate the features of strain
125 variation through sample A8B described below (Figure 2c, Table 1). The sample is cut in the X-
126 Z section of the kinematic reference frame. Where minerals have been abbreviated, we follow
127 the database from Whitney & Evans (2010).

128

129 *3.1 Electron microscopy*

130 Electron probe microanalysis was carried out at CAMPARIS (Sorbonne University, Paris,
131 France) using a Cameca SX-Five instrument. Point measurements were made using 15 kV
132 accelerating voltage, a 10 nA beam current with a 1 μm spot size. Composition maps were
133 acquired using a 15 kV accelerating voltage, a 40 nA beam current with a 1 μm spot size and
134 50 ms dwell time. The instrument was calibrated using diopside (Ca, Mg, Si), MnTiO₃ (Mn, Ti),
135 orthoclase (K, Al), Fe₂O₃ (Fe), albite (Na) and Cr₂O₃ (Cr) as standards to measure elements in

136 brackets. Selected representative analyses of garnet, clinopyroxene, plagioclase and
137 amphibole from point analysis are shown in Table 2.

138

139 3.2 *Thermodynamic modelling and empirical thermo-barometry*

140 Several empirical thermo-barometers were used to estimate the pressure-temperature
141 conditions of formation of the mineral assemblages observed in the low, mid and high strain
142 zones. The crystallization temperatures of metamorphic garnet and clinopyroxene pairs at
143 microstructural equilibrium were estimated using the thermometer of Powell (1985). For
144 these estimates, pressure was taken to be ~1 GPa - a conservative assumption as garnet-
145 clinopyroxene thermometry is poorly dependent on pressure (pressure variations of 0.5 GPa
146 affect the temperature by $\leq 15^{\circ}\text{C}$). The crystallization temperatures of amphibole and
147 plagioclase pairs were calculated using the combined thermo-barometers of Holland & Blundy
148 (1994) and Molina *et al.* (2015).

149 In addition, forward thermodynamic modelling (Perple_X software version 6.8.6; (Connolly &
150 Kerrick 1987, Connolly 2009) were conducted to estimate the pressure-temperature
151 conditions of the high strain layers. In contrast to the low and mid strain domains, the high
152 strain domain showed clear criteria of chemical equilibrium. The pseudosection was modelled
153 in the NCKFMASH system using the internally consistent thermodynamic dataset
154 (hp62ver.dat) of Holland & Powell, (2011). The following solution models were used: White *et*
155 *al.* (2014) for orthopyroxene, biotite, chlorite and garnet, Green *et al.* (2016) for mafic melts,
156 augite and hornblende, and Holland & Powell (2003) for plagioclase and K-feldspar. The H₂O
157 value was set to 1.1 wt. % after calculating a T-X(H₂O) diagram with a H₂O content ranging
158 from 0.5 to 2 wt.% (i.e., excess water) at a pressure of 1 GPa, consistent with the estimates

159 from the amphibole-plagioclase thermo-barometry (Figure S1, Table S1; Holland & Blundy
160 1994, Molina *et al.* 2015). The H₂O value is also consistent with the proportion of amphibole
161 (~ 50 vol. %) observed in the high strain layers (see section 4.1.3).

162

163 3.3 Electron backscattered diffraction (EBSD)

164 Crystallographic orientation data was collected via electron backscattered diffraction (EBSD)
165 Oxford Instruments Nordlys S detector also on the Zeiss Merlin SEM at the University of
166 Tromsø. Crystallographic data were collected using 20 kV accelerating voltage, 70° specimen
167 tilt angle and 24-29 mm working distance. Detailed maps of ~16 mm² were measured with a
168 step size of 1-3 μm and 7 bands detected. Oxford Instruments Aztec software was used for
169 data acquisition and initial data processing, MTEX v.5.2.8 open source software toolbox
170 (Bachmann *et al.* 2010) for MATLAB was used for enhanced data processing and pole figure
171 plotting. Individual crystal orientations with median absolute deviation (MAD) values >1.0
172 were removed. Individual grains were reconstructed using the 'calcGrains' function in MTEX
173 using a 10° misorientation cut-off relative to neighbouring solutions. Pole Figures were
174 created for the mean orientation of each grain based on the orientation distribution function
175 (ODF), using the 'calcDensity' function within MTEX (Bachmann *et al.* 2010). The mean
176 orientation of each individual grain was then plotted on lower hemisphere, equal area pole
177 figures such that each data point represents a single grain on the pole figure, which are
178 subsequently contoured. Calculated J-indices show the CPO fabric strength (e.g. e.g. Bunge
179 1982, Mainprice and Silver, 1993) and the M-indices shows the misorientation index (e.g.
180 Skemer *et al.*, 2005).

181

182 3.4 Grain shape parameters

183 Grain size and shape parameters are measured using grains calculated from the EBSD map
184 data as described above with a misorientation threshold of 10° . The grain size is calculated via
185 the equivalent radius (derived from the grain area) and multiplied by 2 to yield the grain size.
186 The grain data for low, mid and high strain areas have been grouped together to give an
187 overview of grain shape parameters in each of the strain zones (see Table 1 for strain
188 domains). The histogram has $5\ \mu\text{m}$ bin sizes and shows grain sizes up to $500\ \mu\text{m}$ (larger grains
189 are present in the samples but low in quantity). Grain statistics for mean, median, mode (range
190 of largest bin) and standard deviation are shown alongside the grain size histogram data in.
191 Grain orientation is calculated using a fitted ellipse and orientation of the long axis.

192

193 4. Results

194 4.1 Sample description

195 The outcrop displays strain gradients with weakly deformed low strain domains (5-20 cm in
196 height, 20-40 cm in length) that are bound by high strain mylonites (Figure 2). Even in the less
197 deformed domains, the original gabbroic fabric described by Getsinger *et al.* (2013; c.700 m
198 east) is not or only partially preserved (Figure 2). Mid-strain domains show segregation of
199 mafic and plagioclase-derived minerals, and this distinction develops into thin layers in most
200 high strain zones (Figure 2c). Below, we present the results for microstructures, chemical
201 properties and crystallographic preferred orientation (CPO) of each type of domain (low, mid
202 and high strain zones). Strain domains present in each thin section and EBSD map are
203 summarised in Table 1.

204 The heterogeneous strain distribution typically shows the highest strain parts between lower
205 strain parts. Such a strain distribution is interpreted as a narrowing of shear zones caused by
206 progressive localization of deformation (type 2 shear zone; Means 1995). This interpretation
207 implies that lower strain regions preserve earlier stages and the highest strain regions the last
208 stages of the deformation history.

209

210 *4.1.1 Low strain zones*

211 The primary phases in the low strain zones are clinopyroxene and plagioclase with minor
212 orthopyroxene, amphibole ilmenite and zoisite (Figure 3a). The original igneous gabbro
213 assemblage has been metamorphosed; original pyroxene porphyroclasts (referred to as cpx_1)
214 are surrounded by a mixing of secondary pyroxene (cpx_2) and amphibole (amp_A) grains
215 forming corona rim structures. New plagioclase grains (pl_2) replace original plagioclase grains
216 (pl_1 ; Figure 4a-c, 6c).

217 The cpx_1 grains are much larger in size (3-6 mm) than the cpx_2 grains ($< 200 \mu m$). The cpx_1
218 show undulose extinction and thin lamellae of ilmenite and amphibole reaction products
219 (amp_A) along cpx_1 cleavage planes/cracks (Figures 3a-b, 4a-b). Some large cpx_1 grains have
220 neo-crystallized portions that follow larger cleavage cracks in the original grain; these are
221 composed of both cpx_2 and amp_A (Figure 4a-b).

222 The amp_A grains have a larger grain size in the cpx_1 strain pressure shadows, 50 vs. 100 μm
223 (Figure 4a-f, 5a). Shape and size analysis of amphibole grains show a unimodal grain size
224 distribution with a mean grain size of 68 μm and grains are elongated parallel to the foliation
225 (Figure 5a, d). The orthopyroxene grains have also been replaced by amphibole; the few relicts
226 that remain are fully recrystallized (Figure 3a).

227 The original pl₁ grains are up to 3 mm with undulose extinction. They generally include zoisite
228 needles up to 400 µm in length (Figure 4b-c, 6c). The later neo-crystallized pl₂ grains are
229 recrystallized 50-300 µm in size and show straight extinction and ~120° triple junctions
230 (Figure 4b-c). The plagioclase domains typically appear more deformed than the pyroxene
231 domains and form a weak foliation.

232 Ilmenite is found adjacent to clinopyroxene grains and often exhibits amphibole or garnet
233 coronas rims (Figure 3a, 4d). Olivine is not found in the A8B sample, but it is present in
234 undeformed gabbro ~700 m east as detailed by Getsinger *et al.* (2013).

235

236 4.1.2 Mid strain zones

237 Towards the margins of the gabbro pods, the foliation is progressively stronger in intensity
238 (Figure 3b). Clinopyroxene, plagioclase and amphibole are the dominant phases with minor
239 amounts of garnet, zoisite, quartz and ilmenite whilst orthopyroxene is not present. Corona
240 structures are ubiquitous and grade into elongated tails at the ends of porphyroclasts defining
241 the foliation.

242 Cpx₁ grains represent the primary grains and are 0.5-2 mm in size (smaller than in the low
243 strain areas of the rock). The primary cpx₁ grains have undulose extinction and the thin
244 lamellae of amp_A along cpx₁ cleavage planes can be recrystallized as 'blebs'. The recrystallized
245 tails consisting of new grains of cpx₃ have a granoblastic texture without signs of internal grain
246 deformation (top right of Figures 4d, 5b-c).

247 The amp_A grains that surround both cpx₁ grains and cpx₂ grains from recrystallized tails are
248 coarser than in low strain domains, up to 200 µm. Quartz is present in trace volumes between

249 some cpx_1 grains and their surrounding amp_A rims (Figure 6c). There are zones where
250 amphibole (amp_B) has almost completely replaced the cpx_1 (e.g. amp_{B2} zone in Figure 4f). In
251 these elongated zones of bands the amp_B grain size is up to 500 μm . Within these bands, there
252 are minor amounts of clinopyroxene, quartz and ilmenite. Despite the observed grain size
253 increase in amphibole, the average grain size is only 64 μm as there is a high proportion of
254 small amp_A grains associated with the clinopyroxene replacement (cpx_2 ; Figure 4d-f, 5b).

255 Similarly to the cpx_1 , the large pl_1 grains are smaller in the mid strain zone (up to 2 mm),
256 although still exhibit undulose extinction and deformation bands. The recrystallized pl_2 grains
257 show little internal deformation. Some grain boundaries are more lobate than in the low strain
258 zones (Figure 4e, 6c). The amphibole and plagioclase grains in the mid strain areas are
259 orientated with their long axes parallel to the foliation (Figure 5e). Prismatic zoisite is up to
260 500 μm in length within large pl_1 grains where they are loosely aligned to the foliation but
261 zoisite is also present in the smaller pl_1 grains with a random orientation (Figure 4c, e). In some
262 mid strain regions garnet grows in bands after cpx_1 , pl_1 and ilmenite, the grains are up to 100
263 μm in size, are faceted and have equant shape with quartz inclusions (Figure 4d-e).

264

265 *4.1.3 High strain zones*

266 In several layers around the gabbro pods and in between the mid strain zones, there are high
267 strain zones, where the rock is strongly deformed and appears mylonitic in the field (Figure 2).
268 The foliation is well developed in the high strain zones exhibiting alternating bands of
269 amphibole and plagioclase with occasional garnet bands (Figure 3c). The amp_B bands have
270 trace amounts of clinopyroxene, quartz, calcite, and ilmenite interspersed (Figure 4g-i).

271 The amp_B grains are up to 600 μm in length with a mean grain size of 91 μm (Figure 5c).
272 Amphibole in layers associated with garnet and ilmenite are olive green (amp_{B1}) in colour
273 under plane polarized light, compared to amphibole layers with low volumes of minor
274 minerals that are jade green (amp_{B2}) in colour (Figure 4g-i). Amphibole shows the strongest
275 SPO of the differently strained zones with grains strongly orientated parallel to the shear
276 direction, and also to the foliation (Figure 5f).

277 The pl_2 bands are recrystallized and no longer contain any of relicts of original pl_1 grains
278 (porphyroclasts; Figure 4g-i). Pl_2 is also present in mixed bands with amp_B , forming polyphase
279 layers (Figure 4i). In such layers, the mean plagioclase grain size is decreased to 83 μm and the
280 grain size distribution is virtually identical to amphibole (Figure 5c). The plagioclase grains
281 show a similar long axis orientation in the mid and high strain areas (Figure 5 e-f).

282 Quartz is present as interstitial blebs and inclusions within amphibole and plagioclase. Calcite
283 and ilmenite are both cusped in shape. Zoisite is rarely present in high strain zones. When
284 found it is less than 20 μm long and randomly orientated (Figure 4h). Garnet bands up to 4
285 mm in width are commonly associated with amphibole-plagioclase band alternation (Figure
286 4g). Isolated garnet grains are also present within amphibole layers. The garnets are
287 subhedral, typically 1-3 mm in size and are associated with quartz and calcite. Quartz is
288 present as inclusions and interstitial blebs in the garnet whilst calcite is interstitial forming
289 cusped shapes around the garnets (Figure 4g, 6b).

290

291 *4.2 Mineral chemistry*

292 Clinopyroxene has a diopside-rich composition with a $\text{Mg}\#$ [$\text{Mg}/(\text{Mg}+\text{Fe})$] ranging between
293 0.65 and 0.80 (Figure 6a, Table 2). Magmatic porphyroclasts of cpx_1 (samples A8B1, A8B4)

294 show higher values (0.75-0.80) than new small cpx₂ grains at their rims and tails (0.75-0.72).
295 New metamorphic cpx₃ grains scattered in the matrix (sample A8B4) show the lowest Mg#
296 values (0.65-0.73). The amount of Na, representing the jadeite content, varies between 0.3
297 and 0.5 a.p.f.u. regardless of the microstructural position. The changes in Mg and Na content
298 are illustrated in Figure 6a-b, new small grains surrounding or forming tails around magmatic
299 cpx₁ porphyroclasts have lower MgO and higher Na₂O value than the original cpx₁ grains. All
300 chemical analyses are available in Table 2.

301 Amphibole analyses plot within the pargasite to actinolite fields (nomenclature from Leake *et*
302 *al.* 1997; Figure 7b). The Mg# varies between 0.50 and 0.75, and the Ti ranges up to 0.25 a.p.f.u.
303 (Figure 7c, Table 2). The Mg# shows a continuous increase, and the Ti a continuous decrease
304 versus increasing Si, with clear microstructural relations (Figure 6). Amp_A crystallizing after the
305 magmatic cpx₁ porphyroclasts in the low and mid strain zones (samples A8B1, A8B4) has the
306 highest Mg# (> 0.60) and Si values (> 6.6 a.p.f.u.) and the lowest Ti content (< 0.1 a.p.f.u.). In
307 the low, mid and high strain zones, amp_B co-existing with pl₂ has lower Mg# (<0.63) and Si
308 values (<6.6 a.p.f.u) with generally higher Ti content (0.06-0.16 a.p.f.u.). While amp_C included
309 in garnet in the mid strain zone has the same composition as amp_B in the plagioclase-rich
310 layers, amp_D included in garnet in the high strain zone shows the highest Ti content (0.12-
311 0.24).

312 The plagioclase has an anorthite content [Ca/(Ca+Na)] varying between 0.25 and 0.60 (Figure
313 7d). A correlation is observed with both microstructural position and fabric intensity. In the
314 low (A8B1) and mid (A8B4) strain zone, the cores of magmatic pl₁ porphyroclasts (Figure 6a)
315 have the highest anorthite content (0.54-0.60). The porphyroclast rims and new small grains
316 of pl₂ at microstructural equilibrium with amp_B in such samples (Figure 6a, c) show an

317 intermediate composition (values of 0.35-0.55). A similar distribution is observed for the new
318 recrystallized pl_2 grains equilibrated with amp_B in the high strain zone (e.g. mixed $amp-pl$
319 bands in Figures 4h-c, 11c), varying from 0.28 to 0.45. Pl_3 in the garnet-amphibole bearing
320 layers from the mid and high strain zones (samples A8B4, A8B9) have the lowest anorthite
321 content (0.25-0.40).

322 The garnet chemical composition in the amphibole-free layers of the mid strain zones varies
323 in function of the neighbouring minerals (Figure 6 c, 7e-f). Regions near crystal faces next to
324 clinopyroxene are enriched in Fe and Mg (Alm: 0.59, Prp: 0.15, Grs: 0.23, Sps: 0.02) while
325 regions near faces next to plagioclase are enriched in Ca (Alm: 0.51, Prp: 0.10, Grs: 0.36, Sps:
326 0.02). Mn content remains low regardless of the neighbouring minerals. Garnet in the $amp_{C/D}$ -
327 rich layers of the high-strain zones shows a more homogeneous composition (Alm: 0.53-0.57,
328 Prp: 0.13-0.14, Grs: 0.25-0.29, Sps: 0.05) that lies in-between the two garnet compositions
329 recognized in the mid-strain zones.

330 Mineral chemistry exhibits local microstructural variations within the gabbro. For example,
331 Figures 6a-b and 7a show the variation in Mg-content between cpx_1 porphyroclasts and
332 adjacent new cpx_2 grains. The garnet grain B in Figure 7e shows how garnet chemistry varies
333 when adjacent either to clinopyroxene or to plagioclase. The garnet rim around a
334 clinopyroxene grain shows a variation in Mg content (Figure 6c); when adjacent to plagioclase
335 it is more depleted than the core which is adjacent to clinopyroxene and ilmenite. Figure 6d
336 shows a chemical map in a high strain amphibole area and how the chemistry varies between
337 the olive green (amp_{B1} , top) and jade green (amp_{B2} , bottom) coloured amphibole (e.g. Figure
338 4h-i); the olive green coloured amp_{B1} has higher Mg and Si values compared to the jade green

339 coloured amp_{B2}. In addition the olive green coloured amp_{B1} exhibits zoning, with a decreasing
340 of Mg and Si content from core to rim.

341

342 4.3 Pressure-temperature estimates

343 The amphibole-plagioclase thermo-barometry (Holland & Blundy 1994, Molina *et al.* 2015)
344 yielded results for three samples of the low, mid and high strain zones (samples A8B1, A8B4
345 and A8B9, respectively; Table S1). The amp_B-pl₂ pairs were chosen based on textural evidence
346 of equilibrium: immediately adjacent analyses along straight grain boundaries. The results
347 indicate similar P-T conditions of $690 \pm 25^\circ\text{C}$ and 1.05 ± 0.15 GPa for all domains (Figure 8
348 inset, Table S1). Crystallization temperatures in the mid strain zone were also calculated using
349 the garnet-clinopyroxene thermometer of Powell (1985) and Krogh (1988; Table S2).
350 Metamorphic pairs at textural equilibrium (Mg-Fe-rich garnet and cpx₂; Figure 6c) at textural
351 equilibrium yielded $700 \pm 25^\circ\text{C}$ at 1 GPa (Figure 8 inset).

352 Peak P-T conditions of the high strain zone were additionally constrained through
353 thermodynamic modelling. The best fit of the garnet, amphibole and plagioclase isopleths lie
354 in the field with Amph + Cpx + Grt + Pl + Qz (without free-water), around $675 \pm 25^\circ\text{C}$ and 1.05
355 ± 0.05 GPa (Figure 8). The predicted mineral compositions of plagioclase, amphibole and
356 garnet match those documented by mineral analyses in this study. The modelled
357 temperatures and pressures are in very good agreement with those of the conventional
358 thermo-barometry.

359

360 4.4 Crystallographic preferred orientation (CPO)

361 Figure 9 shows lineation-parallel (= X-pole-figure-axis) amphibole orientation maps, CPO pole
362 figures, and inverse pole figures (IPF) of amphibole and clinopyroxene. Clinopyroxene CPO's
363 are only shown for low and mid strain areas as there are insufficient grains in the high strain
364 areas to construct statistically meaningful pole figures. All individual phase maps and CPO pole
365 figures for amphibole, clinopyroxene, plagioclase, quartz, calcite and ilmenite are available in
366 supplementary information (Figure S2-6).

367 In the low strain areas, amphibole CPO is characterised with poles to the (100) subnormal to
368 the shear plane (XY-pole figure-section; Figure 9), and the [001] axes subparallel to the shear
369 direction (X-axis). The amphibole J-index is 8.26 and the M-index is 0.284 for the example low
370 strain zone (A8B1). The misorientation axes for amphibole subgrains (2-10°) show maxima
371 around [001] and account for >25% of misorientations (Figure 9d). When the clinopyroxene
372 CPO is considered alongside the amphibole CPO, the maxima are weaker but they are
373 orientated in similar directions. The misorientation axes for clinopyroxene subgrains is very
374 strong around [001] and accounts for 50% of the total misorientation.

375 In the mid strain area the amphibole CPO has a similar fabric to the low strain area; poles to
376 the (100) plane are subnormal to the shear plane, and the [001] axes is subparallel to the shear
377 direction (Figure 9). The [001] axes shows a weaker maximum but are aligned closer to the
378 shear direction than the fabric in the low strain areas. For the mid strain zone, the amphibole
379 J-index is 3.33 and the M-index is 0.111 (A8B4). The subgrain misorientation axes are weakly
380 distributed between [001] and [-100], with the highest frequency of misorientations
381 associated with subgrains. The clinopyroxene CPO in the mid strain areas is very weak and
382 does not correlate to the amphibole CPO (Figure 9).

383 In the high strain region (A8B9), the amphibole CPO exhibits a weak girdle and maximum of
384 poles to (100) orientated normal to the shear plane, poles to (010) planes in a weak maximum
385 subnormal to the foliation and the shear direction and the [001] direction shows a strong
386 maximum parallel to the shear direction (Figure 9). The amphibole J-index is 4.25 and the M-
387 index is 0.128 for the high strain area. The amphibole subgrain misorientation axes is strong
388 around [001] and accounts for >20% of misorientations (Figure 9d).

389 The relationship between the amphibole and clinopyroxene CPO is further explored in Figure
390 10 where four regions of a clinopyroxene grain with amphibole replacement has been studied.
391 Region A shows the CPO for the clinopyroxene grain (cpx_1) and all surrounding amphibole
392 grains. This amphibole CPO is weak and the maxima are directly related to maxima in the
393 clinopyroxene CPO. Region B focusses on the left hand side of the main clinopyroxene grain
394 ($cpx_{1/2}$), which has undergone more recrystallization than the right. The CPO is almost identical
395 to region A, but is much stronger (for clinopyroxene and amphibole) than in region B. Region
396 C shows the CPO for the right hand side of the clinopyroxene grain (cpx_1) and the amphibole
397 (amp_A) inclusions within the grain. The CPO for this area is very strong, the amphibole and
398 clinopyroxene maxima are in identical positions and are similar to the CPOs observed in
399 regions A and B. The final area, region D, considers the tail of the clinopyroxene (cpx_2) where
400 the highest amount of recrystallization and deformation has occurred. The clinopyroxene CPO
401 for region D is very weak and does not bare a strong resemblance to the amphibole CPO. The
402 amphibole CPO in region D is similar to the whole map amphibole CPO (region A) in the mid
403 strain area in Figure 9b.

404 The plagioclase CPO is generally weak; in low strain regions there tends to be a very weak CPO
405 (Figure 11a) but the CPO is not consistent between different low strain maps (see Figure S5).

406 The high strain area was analysed in subsets to see if there is a change in CPO strength
407 between monophasic and polyphasic regions (Figure 11c; e.g. Mehl & Hirth 2008). The CPO is
408 weak and shows no fabric in any of the subsets, for plagioclase. Nevertheless, the amphibole
409 for this (and all other) high strain areas shows a strong CPO with (001) normal to the shear
410 direction and [001] parallel. The plagioclase CPO is also weak in the mid strain zone.

411 The quartz, calcite and ilmenite show disordered CPOs, they are either weak or strongly
412 dominated by a few grains. Pole figures for these minerals are found in supplementary figures
413 S6.

414

415 5. Discussion

416 The Kågen gabbro is a 45 km² intrusion with a relatively unaltered and undeformed core.
417 Deformation increases towards its margins with the Vaddas Nappe. The southern coastline of
418 Arnøya provides a transect through the gabbro. The centre of the gabbro is relatively
419 undeformed with a clinopyroxene, olivine, and plagioclase (\pm orthopyroxene) assemblage
420 (Getsinger *et al.* 2013). There is localised deformation in the core of the gabbro where it is
421 cross-cut by fluid-rich pegmatites. The deformation in the immediate vicinity to pegmatites is
422 related to fluid released during pegmatite emplacement, the late magmatic stage of the
423 gabbro intrusion (Getsinger *et al.* 2013).

424 Towards the edges of the gabbro (best exposed in the west), lenses of weakly deformed
425 gabbro are surrounded by high strain margins; representing a small scale version of the
426 general strain distribution of the whole gabbro body. The deformation at the gabbro margins
427 overprints the largely undeformed gabbro body. This suggests the centre of the gabbro did
428 not experience deformation during this deformation phase, it remained strong and rigid,

429 whilst heterogeneities produced by local mineral reactions at the margins were exploited to
 430 localise deformation during emplacement of the Vaddas Nappe (Getsinger *et al.* 2013, Faber
 431 *et al.* 2019).

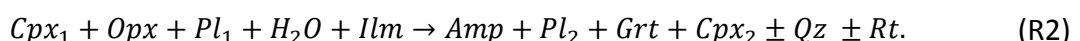
432

433 5.1 Mineral reactions and P-T-time of deformation

434 Getsinger *et al.* (2013) studied intrusion related deformation within the centre of the Kågen
 435 Gabbro, and observed an assemblage similar to the low strain areas in this study. The
 436 undeformed gabbro of Getsinger *et al.* (2013) has higher volumes of olivine and
 437 clinopyroxene, and the amphibole corona rims are absent or not well developed.
 438 Clinopyroxene is the main mafic phase of the gabbro. According to Getsinger *et al.* (2013)
 439 orthopyroxene in the undeformed gabbro is commonly associated with the olivine and has
 440 formed as reaction rims around it. Therefore, it is suggested that the initial alteration of the
 441 gabbro occurred via olivine reacting with plagioclase forming pyroxene (plus some spinel)
 442 rims:



443 Metamorphism of the margins of the Kågen gabbro likely occurred during emplacement and
 444 deformation of the Vaddas nappe. This main deformation event resulted in a pyroxene
 445 consuming and amphibole producing hydration reaction during nappe emplacement under
 446 changed pressure and temperature conditions:



447 The least deformed parts of the Kågen gabbro exhibit some preserved assemblages (left hand
 448 side of Reaction R1) and some reacted products (right hand side of Reaction R1). The high

449 strain regions at the margins represent the final assemblage in Reaction R2 (right hand side of
450 R2). The low and mid strain areas show the progression of the mineral reaction R2 which is
451 synchronous with deformation. There are remnants of clinopyroxene within some high strain
452 amphibole layers; they represent former clinopyroxene grains that were not fully consumed
453 in the amphibole producing reaction.

454 Mineral segregations show a heterogeneous distribution of reaction products, this
455 relationship can occur through dissolution-reprecipitation (Robin 1979), poly-phase GBS
456 (Hiraga *et al.* 2013) and nucleation of reaction products at microstructural or crystallographic
457 sites associated with the reactant (Moore *et al.* 2015). In this study, thermodynamic modelling
458 combined with conventional thermo-barometry show that reaction R2 took place at 690 ± 25
459 $^{\circ}\text{C}$ and 1.05 ± 0.15 GPa (within the uncertainties of the methods; Figure 8), which overlaps
460 previously established P-T conditions for the solid state cooling of the gabbro ($650\text{-}900^{\circ}\text{C}$, 0.7-
461 0.9 GPa; Getsinger *et al.* 2013). Amphibole-plagioclase pairs show similar P-T conditions for
462 the low, mid and high strain zones (Figure 8 inset, Table S1). Such a result indicates that the
463 progression of mineral reactions were directly dependent on changes in H_2O content in the
464 bulk rock rather than a change in P-T conditions during deformation (Finch *et al.* 2016, Giuntoli
465 *et al.* 2018, Whyte *et al.* 2021).

466 Generally, in mid strain areas, the clinopyroxene is elongated and partially overgrown (Figure
467 4f bottom) or completely replaced (Figure 4f top) by elongated amphibole. However, in some
468 areas the amphibole rims are absent and the clinopyroxene is mantled by garnet and
469 occasional ilmenite (Figure 4d-e). The absence of amphibole, a hydrated mineral, in these
470 regions indicates a limited aqueous fluid. These observed microstructural differences together
471 with the presence of corona structures demonstrate that local equilibrium has prevailed, most

472 likely because fluid availability in the gabbro is extremely localised, and therefore reaction R2
473 is incomplete in the fluid-deficient parts. In those parts where reaction R2 is complete, as is
474 the case for the high strain zones, aqueous fluids must have been more abundant, and
475 therefore we suggest the high strain zones (which have formed after the low and mid strain
476 zones) had formed fluid pathways. It is unlikely that these pathways have exploited pre-
477 existing features in the gabbro (e.g. Mancktelow & Pennacchioni 2005, Pennacchioni &
478 Mancktelow 2018, Ceccato *et al.* 2020), because such features have been interpreted as
479 mineralised veins leading to a different type of shear zones described by Getsinger *et al.*
480 (2013). Essentially, the gabbro deformation was facilitated by mineral reactions, which in turn
481 are facilitated by fluid transport and availability, i.e. an in-situ interaction of deformation and
482 reaction (Rutter & Brodie 1985, Fitz Gerald & Stünitz 1993, Stünitz & Fitz Gerald 1993).

483 The change in chemistry of new (cpx_2) vs. magmatic (cpx_1) clinopyroxene grains and the
484 change in amphibole ($\text{amp}_{\text{A-D}}$) chemistry when it neighbours different minerals (e.g.
485 clinopyroxene, plagioclase or garnet), demonstrates that metamorphic reactions
486 accompanied deformation (Figure 6, 7). New cpx_2 grains have a different chemical
487 composition from that of the cpx_1 porphyroclasts, indicating homogeneous nucleation.
488 Nucleation of new cpx_2 with a different chemistry is a response to the change in P-T conditions
489 since gabbro emplacement. The cpx_1 becomes unstable as aqueous fluid infiltrates the gabbro
490 and enhances reaction R2. One of the consequences of the reaction-enhanced deformation is
491 strain localisation (e.g. Rutter & Brodie 1985, Mansard *et al.* 2020a, 2020b). The zoning of
492 amp_{B1} grains shows that it grew during a synkinematic reaction (Figure 6d). The change in
493 mineral chemistry within or between neighbouring grains demonstrates that there has been
494 local equilibrium between phases, most likely due to local variations in fluid availability.
495 Mineral chemistry variations in the low and mid strain zones are associated with

496 microstructural deformation features indicating that the dominant driving potential for
497 crystallization of clinopyroxene and amphibole has been (local) chemical equilibrium and not
498 internal strain energy, i.e., dynamic recrystallization was not the dominant process for
499 reconstituting the microstructures (e.g. Stünitz 1998, Okudaira *et al.* 2015, Giuntoli *et al.* 2018,
500 Soret *et al.* 2019, Mansard *et al.* 2020a, 2020b). When the P-T conditions for the high strain
501 areas Kågen gabbro margins (this study) and those of the more preserved inner parts of the
502 gabbro (Getsinger *et al.* 2013) are considered in relationship to the surrounding Vaddas Nappe
503 metasediments (Faber *et al.* 2019), the results from this study lie on a P-T path connecting
504 them (Figure 12). This suggests the margins of the Kågen gabbro may record the conditions
505 for early stages of Vaddas Nappe thrusting after the gabbro emplacement, which took place
506 at 439 ± 1 Ma (Faber *et al.* 2019). The deformation observed in this study is part of the same
507 event as the deformation of the metasediments at the Vaddas-Kalak boundary (432 ± 6 Ma,
508 $^{206}\text{Pb}/^{238}\text{U}$ ages; Faber *et al.* 2019), and the timing of the deformation of the gabbro margins
509 can be constrained as between ca. 440-432 Ma.

510

511 5.2 Formation of crystallographic preferred orientation (CPO)

512 During deformation and metamorphism of the Kågen gabbro, the clinopyroxene CPO
513 weakened as it destabilised, whilst the amphibole fabric strengthened as it precipitated
514 (Figure 9-10). Amp_A nucleation within cpx_1 grains in the low and mid strain areas indicate that
515 initially amp_A replaced cpx_1 topotactically along cleavage planes (Figures 4a-b, 4e, 9a-b, 10c;
516 e.g. Shannon & Rossi 1964, Handy & Stünitz 2002, McNamara *et al.* 2012, Moore *et al.* 2015).
517 The initial topotactic replacement of cpx_1 by amp_A resulted in a direct inheritance of the cpx_1
518 CPO (Figure 10) and a smaller mean grain size in low strain areas (Figure 5a). A similar situation

519 is inferred for the initial corona rims of amphibole on cpx_1 . Thus, regions B and C in Figure 10
520 show strong CPO maxima for amphibole that do not relate to the shear geometry but are
521 instead orientated closely to that of the host clinopyroxene grain.

522 The amphibole fabric evolved to an orientated growth fabric that is parallel to the shear
523 direction. The growth character of the fabric is shown by the SPO strength increasing from low
524 to high strain areas (Figure 5 d-f). If we consider regions A and D in Figure 10 (including the
525 amphibole rim and tail surrounding relict cpx_1 grain(s) and new cpx_2 grains); the poles to the
526 (100) plane of amphibole becomes orientated subnormal to the shear direction, and the
527 amphibole [001] axes orientated subparallel to the shear direction. These orientations do not
528 correlate with the weaker clinopyroxene CPO's, particularly in region D (Figure 10), where the
529 clinopyroxene (cpx_2) CPO is very weak and does not show a distinct fabric. The morphology of
530 the cpx_2 grains in the recrystallized tail in region D is similar to that of dynamic recrystallization
531 during crystal plastic deformation, but chemical analysis shows that these new cpx_2 grains are
532 compositionally different to the original cpx_1 grains (Figure 7a) and must have formed by
533 homogeneous nucleation due to a chemical driving potential. Therefore, we suggest the new
534 cpx_2 grains have primarily formed during the chemical reaction when clinopyroxene adjusts
535 its composition from cpx_1 to cpx_2 . The reaction takes place alongside deformation
536 (accommodated by dissolution-precipitation creep), progressively destroying the
537 clinopyroxene CPO and account for the change in chemistry (e.g. Stünitz 1993, Okudaira *et al.*
538 2015, Marti *et al.* 2017, Stünitz *et al.* 2020, Mansard *et al.* 2020a).

539 Thus, during the subsequent deformation process where amphibole rims and tails develop
540 around cpx_1 grains in the mid strain regions, amp_A started to nucleate on the cpx_1 outer
541 boundaries with the same initial inherited clinopyroxene crystal orientation, but during

542 consumption of the clinopyroxene by reaction, the precipitating amphibole developed a
543 distinct fabric different from the clinopyroxene host-controlled one. The CPO of the amphibole
544 is best interpreted as a growth-controlled fabric. Amphiboles typically are elongated in the c-
545 axis (Deer *et al.* 1997), which is the fastest growth direction. As this [001] direction is aligned
546 with the stretching direction, it is inferred that the amphibole fabric during deformation is a
547 growth-fabric, as inferred by Giuntoli *et al.* (2018) and for omphacite by Stünitz *et al.* (2020).

548 Amphibole ($\text{amp}_{A,B}$) overgrows and precipitates rims and tails around cpx_1 porphyroclasts
549 (Figure 4a-f, 6). The CPO for these tails is progressively less related and therefore less inherited
550 from the clinopyroxene (Figure 10). The SPO strength for amphibole increases from low to
551 high strain areas suggesting amphibole growth in the high strain areas is crystallographic
552 orientation controlled (Figure 5e). In the high strain areas, the amphibole (amp_{B-D}) CPO
553 exhibits a maxima of (100) poles and a weak girdle subnormal to the shear direction and a
554 strong maxima in the [001] axes parallel to the shear direction (e.g. Figure 9). The presence of
555 the girdle in (100) and a very strong SPO parallel to the shear direction suggests a component
556 of rigid body rotation around [001] (Figure 5f, 9c).

557 It is common to observe naturally deformed amphibole with the (100) pole aligned subnormal
558 to the shear plane and the [001] direction aligned subparallel to the shear direction (e.g.
559 Berger & Stünitz 1996, Imon *et al.* 2004, Díaz Aspiroz *et al.* 2007, Tatham *et al.* 2008, Llana-
560 Fúnez & Brown 2012, Getsinger *et al.* 2013, Okudaira *et al.* 2015, Elyaszadeh *et al.* 2018, Soret
561 *et al.* 2019). This fabric has been shown to occur under middle to upper amphibolite facies
562 conditions (650-750°C, 0.6-1 GPa), and commonly shows that amphibole grains are reoriented
563 or grow (sub)parallel to the shear direction (Ko & Jung 2015). The primary slip vector in
564 amphibole is $\langle 001 \rangle$, and a strong amphibole CPO with (100) plane subnormal to foliation and

565 [001] axes parallel to lineation could suggest that (100)<001> easy slip system can be
566 important in generating this type of CPO (Díaz Aspiroz *et al.* 2007). However, in the case of the
567 Kågen gabbro there are no amphibole porphyroclasts, from which the amphibole is
568 recrystallized, so dynamic recrystallization and thus a dislocation creep origin of the
569 amphibole CPO can be excluded.

570 The amphibole CPO observed in the Kågen gabbro is similar to other natural examples, and as
571 amphibole is only present in minor proportions (if at all) in the original gabbro (Getsinger *et*
572 *al.* 2013), we propose that the strong fabric forms during precipitation (homogeneous
573 nucleation) of the amphibole (e.g. Berger & Stünitz 1996, Getsinger & Hirth 2014, Giuntoli *et*
574 *al.* 2018). The weak girdle of (100) poles in the high strain domains indicate minor rigid body
575 rotation occurred around the [001] axes. It has been suggested that such girdles are formed
576 through cataclastic flow forming a fine-grained matrix produced by fracturing and
577 comminution (Imon *et al.* 2004, Kanagawa *et al.* 2008, Kim & Jung 2019). Cataclastic flow is
578 unlikely in these samples, because (a) the confining pressures of ~ 1 GPa make frictional
579 processes unlikely, and (b) the larger and uniform grain size in higher strain domains without
580 evidence for fracturing (Figure 3c, 4c) do not indicate brittle processes. Instead, the rigid body
581 rotation of amphibole grains in the Kågen gabbro is likely to have occurred via progressive
582 rotation in a mechanically weaker plagioclase matrix, facilitated by solution transfer,
583 precipitation and grain growth of the amphiboles as they increase in modal amount.

584 Plagioclase shows a decrease in the mean grain size from low to high strain areas (Figure 5a-
585 c). The larger grain size in low strain areas is due to the preservation of original magmatic pl₁.
586 As deformation of the gabbro progresses, the large original grains are replaced by neo-
587 crystallized plagioclase of a more sodic composition (pl₂; Figure 7d). Unlike the plagioclase

588 studied by Gardner *et al.* (2021) where dissolution-precipitation is identified as the dominant
589 deformation mechanism for plagioclase in a greenschist metagabbro, Ca-plagioclase is
590 preserved in this study. This variation is likely due to a lack of brittle fracturing in the
591 plagioclase preventing complete albitisation. The neo-crystallization also results in a slight
592 elongation of pl₂ grains parallel to the shear direction (Figure 5f). The CPO of new plagioclase
593 is weak, especially in areas where fine plagioclase grain coexist with amphibole (Figure 11;
594 Kruse & Stünitz, 1999; Lapworth *et al.*, 2002; Mehl & Hirth, 2008). In the low strain regions the
595 weak CPO is controlled by large original grains and does not represent a characteristic fabric
596 type of crystal plasticity (Figure 11a; e.g. Getsinger & Hirth 2014). Figure 11c shows that the
597 plagioclase grain size is smaller in the polyphase areas than the monophasic band, suggesting
598 that grain growth is limited in the mixed phase areas. Deformation by diffusion creep in the
599 high strain areas is most likely accommodated by GBS that is localised in polyphase layers
600 where phase mixing occurs between amphibole and plagioclase (Figure 11c, polyphase layer).
601 The weak plagioclase CPO in the high strain areas indicates a lack of crystal plasticity and the
602 dominant deformation mechanism is inferred to be dissolution-precipitation creep (Figure
603 11). Diffusion creep with GBS inhibits development of a CPO and destroys pre-existing CPO's
604 (Elliott 1973). Unlike amphibole, there is not a strong crystallographic control on plagioclase
605 grain shape during precipitation resulting in a lack of CPO (Getsinger & Hirth 2014).
606 Dissolution-precipitation creep is further supported as the primary deformation mechanism
607 active in plagioclase by plagioclase chemistry change from more anorthic in low strain areas
608 to more albitic in high strain zones (Figures 6c, 7d, 11c).

609 Quartz and calcite occur as inclusions in clinopyroxene and garnet grains or interstitially.
610 Quartz is the more common and is usually associated with amphibole and garnet zones. This
611 indicates there was excess silica during the metamorphic reactions to allow quartz

612 precipitation (Figures 6b-d, S2). The lack of CPO fabric in the quartz suggests crystal plastic
613 deformation was not dominant during and post precipitation (Figure S6). Calcite is occurs
614 interstitially with a cusped shape in amphibole zones but more commonly around garnet
615 grains (Figures 6b-c, S2). The cusped calcite morphology and weak CPO fabric suggests it
616 infilled pore space late or after in the deformation (Figure S6). We suggest that these minerals
617 did not undergo any crystal plasticity and precipitated late in the deformation history with no
618 crystallographic orientation controlled growth.

619

620 5.3 Wider implications

621 Deformation of the Kågen gabbro margins is hypothesised to be associated with emplacement
622 of the Vaddas Nappe on a P-T path from 690°C and 1.05 GPa to 630°C and 1.3 GPa (Figure 12a;
623 Faber *et al.* 2019). Crystal plastic deformation may be expected in plagioclase and
624 clinopyroxene at such conditions (Mauler *et al.* 2000, Rybacki & Dresen 2004), however no
625 evidence for dislocation creep processes is observed here. Instead, we observe a change in
626 chemistry and stable phase assemblage between the low and high strain regions (Figure 12b).
627 Fluid pathways within the gabbro allowed metamorphic reactions to proceed and
628 consequently enhanced strain localisation (e.g. Rutter & Brodie 1985, Finch *et al.* 2016, Whyte
629 *et al.* 2021). The fluid supply was limited or infiltration was not pervasive thus allowing
630 preservation of the dry, low strain gabbro pods. During emplacement and deformation of the
631 Vaddas Nappe, the high strain zones formed fluid pathways and a network of anastomosing
632 shear zones that localised deformation and left the low strain areas as dry pods (Figure 2).

633 It is often assumed that new small grains in a deformed rock is the result of dynamic
634 recrystallization (e.g. Tullis & Yund 1992, Stünitz *et al.* 2003), however we show that the new

635 clinopyroxene and plagioclase grains have a different chemistry to the larger original grains
636 (Figure 6, 7). This indicates dissolution-precipitation is responsible for the formation of the
637 new grains rather than a crystal-plastic mechanism. In addition, dislocation creep is
638 considered a fabric strengthening mechanism (e.g. strong CPO) whereas diffusion creep is
639 fabric weakening (e.g. no CPO), but when dissolution-precipitation creep is accompanied by
640 orientated growth, the resultant amphibole CPO is strong. Deformation experiments of
641 plagioclase and pyroxene mixtures by Marti *et al.* (2017, 2018) and Mansard *et al.* (2020a,
642 2020b) showed that amphibole coronas on pyroxene were more elongated in the deformed
643 samples. These results indicate that amphibole has accommodated displacement via
644 dissolution-precipitation creep. As dissolution precipitation creep is a type of diffusion creep,
645 stress exponents for this type of deformation are expected to be as low as those for diffusion
646 creep, i.e. in the order of $n \sim 1$.

647 The processes that control deformation in the Kågen gabbro (e.g. DPC, rigid body rotation and
648 GBS) are similar to those described in the garnet-clinopyroxene amphibolites formed during
649 subduction initiation (Soret *et al.* 2019). Dissolution-precipitation creep alongside amphibole-
650 forming metamorphic reactions in the Kågen gabbro are driven by variations in water activity.
651 Fluid pathways in the gabbro resulted in strain localisation that in turn controlled the rheology
652 (e.g. Marti *et al.* 2017, 2018, Soret *et al.* 2019, Mansard *et al.* 2020a, 2020b). Thus the
653 deformation processes observed in the Kågen gabbro represent common processes
654 controlling the development of hydrated mafic rocks, regardless of the geological setting.

655

656 6. Conclusions

657 Deformation at the margins of the Kågen gabbro on a P-T path from $690^{\circ}\text{C} \pm 25^{\circ}\text{C}$ and
658 pressures of 1.0 to 1.1 GPa provides a natural example of how dissolution precipitation creep
659 facilitates the deformation of mafic rocks during concomitant mineral reactions. The
660 dissolution part of the process takes in the reactants while the precipitation takes place in the
661 new stable product phases. The mechanical properties of mafic rocks during deformation
662 coupled with reactions are substantially weaker than for an assemblage of
663 pyroxene/amphibole and plagioclase without reactions. Through chemical and
664 microstructural analysis we have shown that metamorphic reactions primarily occurred in a
665 fluid-rich environment, which resulted in strain localisation into the hydrating parts of the rock
666 and subsequent weakening as metamorphic reaction progressed. Despite the strong crystal
667 fabric and CPO in amphibole grains, dislocation creep was not the dominant deformation
668 mechanism, instead dissolution-precipitation creep involving both, diffusion-accommodated
669 GBS and diffusive mass transfer, has facilitated the deformation. The CPO is produced by the
670 fastest growth direction and rigid particle rotation, i.e. by shape-factors of the precipitating
671 amphibole. When deformation and mineral reactions occur simultaneously, strong rocks can
672 become mechanically weak, at least transiently. Processes like dissolution-precipitation creep
673 allow the mafic rocks to deform viscously at lower temperatures and lower stresses than
674 expected for dislocation creep of the original constituent phases (pyroxene, amphibole, and
675 plagioclase). Low stress exponents are expected for such a deformation.

676

677 **Acknowledgements**

678 The authors thank Amanda Getsinger for sample collection, documentation, and sample
679 cutting. We thank Jiří Konopásek for discussions and suggestions during early chemical

680 analysis and data processing. We thank Nicolas Rividi (Sorbonne Université, Camparis
681 laboratory, France) for analytical support at the microprobe. We thank Toru Takeshita for
682 editorial handling and the constructive reviews by Alberto Ceccato and Francesco Giuntoli
683 have improved the present version of the manuscript substantially. MB thanks CAPES-Diku
684 Project number 88881.117872/2016-01.

685

686 **Data Availability**

687 EBSD data for maps A8B 2b, 4b, 8a and 9b are available to download as channel text files from
688 <https://doi.org/10.17632/xhd6gs3fyc.1>.

689

690 **7. References**

- 691 Allison, I. & La Tour, T.E. (1977) Brittle Deformation of Hornblende in a Mylonite: a Direct
692 Geometrical Analogue of Ductile Deformation By Translation Gliding. *Can J Earth Sci*,
693 **14**, 1953–1961. doi:10.1139/e77-166
- 694 Andersen, T.B., Austrheim, H., Sturt, B.A., Pedersen, S. & Kjaersrud, K. (1982) Rb-Sr whole
695 rock ages from Mageroy, north Norwegian Caledonides. *Nor. Geol. Tidsskr.*, **62**, 79–85.
- 696 Babaie, H.A. & La Tour, T.E. (1994) Semibrittle and cataclastic deformation of hornblende-
697 quartz rocks in a ductile shear zone. *Tectonophysics*, **229**, 19–30. doi:10.1016/0040-
698 1951(94)90003-5
- 699 Bachmann, F., Hielscher, R. & Schaeben, H. (2010) Texture analysis with MTEX- Free and
700 open source software toolbox. *Solid State Phenom.*, **160**, 63–68.
701 doi:10.4028/www.scientific.net/SSP.160.63
- 702 Berger, A. & Stünitz, H. (1996) Deformation mechanisms and reaction of hornblende:
703 Examples from the Bergell tonalite (Central Alps). *Tectonophysics*, **257**, 149–174.
704 doi:10.1016/0040-1951(95)00125-5
- 705 Biermann, C. & Roermund, H.L.M. van. (1983) Defect structures in naturally deformed
706 clinoamphiboles - a TEM study. *Tectonophysics*, **95**, 267–278.
- 707 Brodie, K.H. & Rutter, E.H. (1985) On the relationship between deformation and
708 metamorphism, with special reference to the behavior of basic rocks. *Metamorph.*
709 *React. Kinet. Textures, Deform.*, 138–179. doi:10.1007/978-1-4612-5066-1_6
- 710 Bunge, H. J.: Texture Analysis in Materials Sciences, Butterworth, London, 1982.

- 711 Bystricky, M. & Mackwell, S. (2001) Creep of dry clinopyroxene aggregates with deformation
712 in the dislocation creep. *J. Geophys. Res.*, **106**, 13443–13454.
- 713 Carter, N.L. & Ave'Lallemant, H.G. (1970) High temperature flow of dunite and peridotite.
714 *Geol. Soc. Am. Bull.*, **81**, 2181–2202.
- 715 Ceccato, A., Goncalves, P. & Pennacchioni, G. (2020) Temperature, fluid content and
716 rheology of localized ductile shear zones in subsolidus cooling plutons. *J. Metamorph.*
717 *Geol.*, **38**, 881–903. doi:10.1111/jmg.12553
- 718 Connolly, J.A.D. (2009) The geodynamic equation of state: What and how. *Geochemistry,*
719 *Geophys. Geosystems*, **10**. doi:10.1029/2009GC002540
- 720 Connolly, J.A.D. & Kerrick, D.M. (1987) An algorithm and computer program for calculating
721 composition phase diagrams. *Calphad*, **11**, 1–55. doi:10.1016/0364-5916(87)90018-6
- 722 Corfu, F., Gasser, D. & Chew, D.M. (2014) New perspectives on the caledonides of
723 scandinavia and related areas: Introduction. *Geol. Soc. Spec. Publ.*, **390**, 1–8.
724 doi:10.1144/SP390.28
- 725 Corfu, F., Torsvik, T.H., Andersen, T.B., Ashwal, L.D., Ramsay, D.M. & Roberts, R.J. (2006)
726 Early Silurian mafic-ultramafic and granitic plutonism in contemporaneous flysch,
727 Magerøy, northern Norway: U-Pb ages and regional significance. *J. Geol. Soc. London.*,
728 **163**, 291–301. doi:10.1144/0016-764905-014
- 729 Cumbest, R.J., Drury, M.R., Roermund, H.L.M. van & Simpson, C. (1989) Dynamic
730 recrystallization and chemical evolution of clinoamphibole from Senja, Norway. *Contrib.*
731 *to Mineral. Petrol.*, **101**, 339–349. doi:10.1007/BF00375318
- 732 Deer, W.A., Howie, R.A. & Zussman, J. (1997) Chain silicates. in *Rock-forming minerals*, pp.

- 733 143–278.
- 734 Díaz Aspiroz, M., Lloyd, G.E. & Fernández, C. (2007) Development of lattice preferred
735 orientation in clinoamphiboles deformed under low-pressure metamorphic conditions.
736 A SEM/EBSD study of metabasites from the Aracena metamorphic belt (SW Spain). *J.*
737 *Struct. Geol.*, **29**, 629–645. doi:10.1016/j.jsg.2006.10.010
- 738 Dimanov, A., Dresen, G., Xiao, X. & Wirth, R. (1999) Grain boundary diffusion creep of
739 synthetic anorthite aggregates: The effect of water. *J. Geophys. Res. Solid Earth*, **104**,
740 10483–10497. doi:10.1029/1998jb900113
- 741 Dimanov, Alexandre & Dresen, G. (2005) Rheology of synthetic anorthite-diopside
742 aggregates: Implications for ductile shear zones. *J. Geophys. Res. Solid Earth*, **110**, 1–24.
743 doi:10.1029/2004JB003431
- 744 Dimanov, Alexandre, Lavie, M.P., Dresen, G., Ingrin, J. & Jaoul, O. (2003) Creep of
745 polycrystalline anorthite and diopside. *J. Geophys. Res. Solid Earth*, **108**.
746 doi:10.1029/2002jb001815
- 747 Dimanov, Alexandre, Raphanel, J. & Dresen, G. (2011) Newtonian flow of heterogeneous
748 synthetic gabbros at high strain: Grain sliding, ductile failure, and contrasting local
749 mechanisms and interactions. *Eur. J. Mineral.*, **23**, 303–322. doi:10.1127/0935-
750 1221/2011/0023-2110
- 751 Dollinger, G. & Blacic, J.D. (1975) Deformation mechanisms in experimentally and naturally
752 deformed amphiboles. *Earth Planet. Sci. Lett.*, **26**, 409–416. doi:10.1016/0012-
753 821X(75)90016-3
- 754 Drury, M.R. & Urai, J.L. (1990) Deformation-related recrystallization processes.

- 755 *Tectonophysics*, **172**, 235–253. doi:10.1109/IMFEDK.2013.6602261
- 756 Elliott, D. (1973) Diffusion flow laws in metamorphic rocks. *Bull. Geol. Soc. Am.*, **84**, 2645–
757 2664. doi:10.1130/0016-7606(1973)84<2645:DFLIMR>2.0.CO;2
- 758 Elyaszadeh, R., Prior, D.J., Sarkarinejad, K. & Mansouri, H. (2018) Different slip systems
759 controlling crystallographic preferred orientation and intracrystalline deformation of
760 amphibole in mylonites from the Neyriz mantle diapir, Iran. *J. Struct. Geol.*, **107**, 38–52,
761 Elsevier. doi:10.1016/j.jsg.2017.11.020
- 762 Faber, C., Stünitz, H., Gasser, D., Jeřábek, P., Kraus, K., Corfu, F., Ravna, E.K., *et al.* (2019)
763 Anticlockwise metamorphic pressure-Temperature paths and nappe stacking in the
764 Reisa Nappe Complex in the Scandinavian Caledonides, northern Norway: Evidence for
765 weakening of lower continental crust before and during continental collision. *Solid*
766 *Earth*, **10**, 117–148. doi:10.5194/se-10-117-2019
- 767 Finch, M.A., Weinberg, R.F. & Hunter, N.J.R. (2016) Water loss and the origin of thick
768 ultramylonites. *Geology*, **44**, 599–602. doi:10.1130/G37972.1
- 769 Fitz Gerald, J.D. & Stünitz, H. (1993) Deformation of granitoids at low metamorphic grade. I:
770 Reactions and grain size reduction. *Tectonophysics*, **221**, 299–324.
- 771 Gardner, J., Wheeler, J. & Mariani, E. (2021) Lithos Interactions between deformation and
772 dissolution-precipitation reactions in plagioclase feldspar at greenschist facies. *Lithos*,
773 **396–397**, 106241, Elsevier B.V. doi:10.1016/j.lithos.2021.106241
- 774 Gasser, D., Jeřábek, P., Faber, C., Stünitz, H., Menegon, L., Corfu, F., Erambert, M., *et al.*
775 (2015) Behaviour of geochronometers and timing of metamorphic reactions during
776 deformation at lower crustal conditions: Phase equilibrium modelling and U-Pb dating

- 777 of zircon, monazite, rutile and titanite from the Kalak Nappe Complex, northern
778 Norway. *J. Metamorph. Geol.*, **33**, 513–534. doi:10.1111/jmg.12131
- 779 Getsinger, A.J. & Hirth, G. (2014) Amphibole fabric formation during diffusion creep and the
780 rheology of shear zones. *Geology*, **42**, 535–538. doi:10.1130/G35327.1
- 781 Getsinger, A.J., Hirth, G., Stünitz, H. & Goergen, E.T. (2013) Influence of water on rheology
782 and strain localization in the lower continental crust. *Geochemistry, Geophys.*
783 *Geosystems*, **14**, 2247–2264. doi:10.1002/ggge.20148
- 784 Giuntoli, F., Menegon, L. & Warren, C.J. (2018) Replacement reactions and deformation by
785 dissolution and precipitation processes in amphibolites. *J. Metamorph. Geol.*, **36**, 1263–
786 1286. doi:10.1111/jmg.12445
- 787 Graziani, R., Larson, K.P. & Soret, M. (2020) The effect of hydrous mineral content on
788 competitive strain localization mechanisms in felsic granulites. *J. Struct. Geol.*, **134**,
789 104015, Elsevier Ltd. doi:10.1016/j.jsg.2020.104015
- 790 Green, E.C.R., White, R.W., Diener, J.F.A., Powell, R., Holland, T. & Palin, R.M. (2016)
791 Activity–composition relations for the calculation of partial melting equilibria in
792 metabasic rocks. *J. Metamorph. Geol.*, **34**, 845–869. doi:10.1111/jmg.12211
- 793 Hacker, B.R. & Christie, J.M. (1990) Brittle/ductile and plastic/cataclastic transitions in
794 experimentally deformed and metamorphosed amphibolite. *Geophys. Monogr.*, **56**,
795 127–147.
- 796 Handy, M.R. & Stünitz, H. (2002) Strain localization by fracturing and reaction weakening -A
797 mechanism for initiating exhumation of subcontinental mantle beneath rifted margins.
798 *Geol. Soc. Spec. Publ.*, **200**, 387–407. doi:10.1144/GSL.SP.2001.200.01.22

- 799 Hiraga, T., Miyazaki, T., Yoshida, H. & Zimmerman, M.E. (2013) Comparison of
800 microstructures in superplastically deformed synthetic materials and natural mylonites:
801 Mineral aggregation via grain boundary sliding. *Geology*, **41**, 959–962.
802 doi:10.1130/G34407.1
- 803 Holland, T. & Blundy, J. (1994) Non-ideal interactions in calcic amphiboles and their bearing
804 on amphibole-plagioclase thermometry. *Contrib. to Mineral. Petrol.*, **116**, 433–447.
805 doi:10.1007/BF00310910
- 806 Holland, T. & Powell, R. (2003) Activity-compositions relations for phases in petrological
807 calculations: An asymmetric multicomponent formulation. *Contrib. to Mineral. Petrol.*,
808 **145**, 492–501. doi:10.1007/s00410-003-0464-z
- 809 Holland, T. & Powell, R. (2011) An improved and extended internally consistent
810 thermodynamic dataset for phases of petrological interest, involving a new equation of
811 state for solids. *J. Metamorph. Geol.*, **29**, 333–383. doi:10.1111/j.1525-
812 1314.2010.00923.x
- 813 Imon, R., Okudaira, T. & Fujimoto, A. (2002) Dissolution and precipitation processes in
814 deformed amphibolites: An example from the ductile shear zone of the Ryoke
815 metamorphic belt, SW Japan. *J. Metamorph. Geol.*, **20**, 297–308. doi:10.1046/j.1525-
816 1314.2002.00367.x
- 817 Imon, R., Okudaira, T. & Kanagawa, K. (2004) Development of shape- and lattice-preferred
818 orientations of amphibole grains during initial cataclastic deformation and subsequent
819 deformation by dissolution-precipitation creep in amphibolites from the Ryoke
820 metamorphic belt, SW Japan. *J. Struct. Geol.*, **26**, 793–805.
821 doi:10.1016/j.jsg.2003.09.004

- 822 Jessell, M.W. (1987) Grain-boundary migration microstructures in a naturally deformed
823 quartzite. *J. Struct. Geol.*, **9**, 1007–1014. doi:10.1016/0191-8141(87)90008-3
- 824 Ji, S., Shao, T., Michibayashi, K., Long, C., Wang, Q., Kondo, Y., Zhao, W., *et al.* (2013) A new
825 calibration of seismic velocities, anisotropy, fabrics, and elastic moduli of amphibole-
826 rich rocks. *J. Geophys. Res. E Planets*, **118**, 4699–4728. doi:10.1002/jgrb.50352
- 827 Kanagawa, K., Shimano, H. & Hiroi, Y. (2008) Mylonitic deformation of gabbro in the lower
828 crust: A case study from the Pankenushi gabbro in the Hidaka metamorphic belt of
829 central Hokkaido, Japan. *J. Struct. Biol.*, **30**, 1150–1166. doi:10.1016/j.jsg.2008.05.007
- 830 Kim, J. & Jung, H. (2019) New Crystal Preferred Orientation of Amphibole Experimentally
831 Found in Simple Shear. *Geophys. Res. Lett.*, **46**, 12996–13005.
832 doi:10.1029/2019GL085189
- 833 Ko, B. & Jung, H. (2015) Crystal preferred orientation of an amphibole experimentally
834 deformed by simple shear. *Nat. Commun.*, **6**, Nature Publishing Group.
835 doi:10.1038/ncomms7586
- 836 Krogh, E.J. (1988) The garnet-clinopyroxene Fe-Mg geothermometer - a reinterpretation of
837 existing experimental data. *Contrib. to Mineral. Petrol.*, **99**, 44–48.
838 doi:10.1007/BF00399364
- 839 Kruse, R. & Stünitz, H. (1999) Deformation mechanisms and phase distribution in mafic high-
840 temperature mylonites from the Jotun Nappe, southern Norway. *Tectonophysics*, **303**,
841 223–249. doi:10.1016/S0040-1951(98)00255-8
- 842 Kruse, R., Stünitz, H. & Kunze, K. (2001) Dynamic recrystallization processes in plagioclase
843 porphyroclasts. *J. Struct. Geol.*, **23**, 1781–1802. doi:10.1016/S0191-8141(01)00030-X

- 844 Langdon, T.G. (2006) Grain boundary sliding revisited: Developments in sliding over four
845 decades. *J. Mater. Sci.*, **41**, 597–609. doi:10.1007/s10853-006-6476-0
- 846 Lapworth, T., Wheeler, J. & Prior, D.J. (2002) The deformation of plagioclase investigated
847 using electron backscatter diffraction crystallographic preferred orientation data. *J.*
848 *Struct. Geol.*, **24**, 387–399. doi:10.1016/S0191-8141(01)00057-8
- 849 Leake, B.E., Woolley, A.R., Arps, C.E.S., Birch, W.D., Gilbert, M.C., Grice, J.D., Hawthorne, F.C.,
850 *et al.* (1997) Nomenclature of amphiboles: Report of the subcommittee on amphiboles
851 of the international mineralogical association, commission on new minerals and mineral
852 names. *Can. Mineral.*, **35**, 219–246.
- 853 Lindahl, I., Stevens, B.P.J. & Zwaan, K.B. (2005) The geology of the Váddás area, Troms: a key
854 to our understanding of the Upper Allochthon in the Caledonides of northern Norway.
855 *Norges Geol. undersøkelse-Bulletin*, **445**, 5–43.
- 856 Llana-Fúnez, S. & Brown, D. (2012) Contribution of crystallographic preferred orientation to
857 seismic anisotropy across a surface analog of the continental Moho at Cabo Ortegal,
858 Spain. *Bull. Geol. Soc. Am.*, **124**, 1495–1513. doi:10.1130/B30568.1
- 859 Lloyd, G.E., Butler, R.W.H., Casey, M., Tatham, D.J. & Mainprice, D. (2011) Constraints on the
860 seismic properties of the middle and lower continental crust. *Geol. Soc. Spec. Publ.*, **360**,
861 7–32. doi:10.1144/SP360.2
- 862 Mainprice, D. & Nicolas, A. (1989) Development of shape and lattice preferred orientations:
863 application to the seismic anisotropy of the lower crust. *J. Struct. Geol.*, **11**, 175–189.
864 doi:10.1016/0191-8141(89)90042-4
- 865 Mainprice, D., & Silver, P.G. (1993) Interpretation of SKS-waves using samples from the

- 866 subcontinental lithosphere. *Physics of the Earth and Planetary Interiors*, **78**(3-4), 257-
867 280. doi:10.1016/0031-9201(93)90160-B
- 868 Mancktelow, N.S. & Pennacchioni, G. (2005) The control of precursor brittle fracture and
869 fluid-rock interaction on the development of single and paired ductile shear zones. *J.*
870 *Struct. Geol.*, **27**, 645–661. doi:10.1016/j.jsg.2004.12.001
- 871 Mansard, N., Stünitz, H., Raimbourg, H. & Pr, J. (2020) The role of deformation-reaction
872 interactions to localize strain in polymineralic rocks : Insights from experimentally
873 deformed plagioclase-pyroxene assemblages, **134**. doi:10.1016/j.jsg.2020.104008
- 874 Mansard, N., Stünitz, H., Raimbourg, H., Précigout, J., Plunder, A. & Nègre, L. (2020)
875 Relationship between microstructures and resistance in mafic assemblages that deform
876 and transform. *Solid Earth*, **11**, 2141–2167. doi:10.5194/se-11-2141-2020
- 877 Marshall, D.B. & McLaren, A.C. (1977) Elastic twinning in experimentally deformed
878 plagioclase feldspars. *Phys. Chem. Miner.*, **41**, 231–240. doi:10.1002/pssa.2210410128
- 879 Marti, S., Stünitz, H., Heilbronner, R., Plümper, O. & Drury, M. (2017) Experimental
880 investigation of the brittle-viscous transition in mafic rocks – Interplay between
881 fracturing , reaction , and viscous deformation. *J. Struct. Geol.*, **105**, 62–79, Elsevier.
882 doi:10.1016/j.jsg.2017.10.011
- 883 Marti, S., Stünitz, H., Heilbronner, R., Plümper, O. & Kilian, R. (2018) Syn-kinematic hydration
884 reactions, grain size reduction, and dissolution-precipitation creep in experimentally
885 deformed plagioclase-pyroxene mixtures. *Solid Earth*, **9**, 985–1009. doi:10.5194/se-9-
886 985-2018
- 887 Mauler, A., Bystricky, M., Kunze, K. & Mackwell, S. (2000) Microstructures and lattice

- 888 preferred orientations in experimentally deformed clinopyroxene aggregates. *J. Struct.*
889 *Geol.*, **22**, 1633–1648. doi:10.1016/S0191-8141(00)00073-0
- 890 McNamara, D.D., Wheeler, J., Pearce, M.A. & Prior, D.J. (2012) Fabrics produced mimetically
891 during static metamorphism in retrogressed eclogites from the Zermatt-Saas zone,
892 Western Italian Alps. *J. Struct. Geol.*, **44**, 167–178, Elsevier Ltd.
893 doi:10.1016/j.jsg.2012.08.006
- 894 Mehl, L. & Hirth, G. (2008) Plagioclase preferred orientation in layered mylonites: Evaluation
895 of flow laws for the lower crust. *J. Geophys. Res. Solid Earth*, **113**, 1–19.
896 doi:10.1029/2007JB005075
- 897 Miranda, E.A., Hirth, G. & John, B.E. (2016) Microstructural evidence for the transition from
898 dislocation creep to dislocation-accommodated grain boundary sliding in naturally
899 deformed plagioclase. *J. Struct. Geol.*, **92**, 30–45, Elsevier Ltd.
900 doi:10.1016/j.jsg.2016.09.002
- 901 Moghadam, H.S., Stern, R.J. & Rahgoshay, M. (2010) The Dehshir ophiolite (central Iran):
902 Geochemical constraints on the origin and evolution of the inner Zagros ophiolite belt.
903 *Bull. Geol. Soc. Am.*, **122**, 1516–1547. doi:10.1130/B30066.1
- 904 Molina, J.F., Moreno, J.A., Castro, A., Rodríguez, C. & Fershtater, G.B. (2015) Calcic
905 amphibole thermobarometry in metamorphic and igneous rocks: New calibrations
906 based on plagioclase/amphibole Al-Si partitioning and amphibole/liquid Mg
907 partitioning. *Lithos*, **232**, 286–305, Elsevier B.V. doi:10.1016/j.lithos.2015.06.027
- 908 Moore, S.J., Cesare, B. & Carlson, W.D. (2015) Epitaxial nucleation of garnet on biotite in the
909 polymetamorphic metapelites surrounding the Vedrette di Ries intrusion (Italian

- 910 Eastern Alps). *Eur. J. Mineral.*, **27**, 5–18. doi:10.1127/ejm/2015/0027-2414
- 911 Morrison-Smith, D.J. (1976) Transmission electron microscopy of experimentally deformed
912 hornblende. *Am. Mineral.*, **61**, 272–280. doi:10.1144/gsjgs.132.3.0343
- 913 Nyman, M.W., Law, R.D. & Smelik, E.A. (1992) Cataclastic deformation mechanism for the
914 development of core-mantle structures in amphibole. *Geology*, **20**, 455–458.
915 doi:10.1130/0091-7613(1992)020<0455:CDMFTD>2.3.CO;2
- 916 Okudaira, T., Jeřábek, P., Stünitz, H. & Füsseis, F. (2015) High-temperature fracturing and
917 subsequent grain-size- sensitive creep in lower crustal gabbros: Evidence for coseismic
918 loading followed by creep during decaying stress in the lower crust? *J. Geophys. Res.*
919 *Solid Earth*, **120**, 3119–3141. doi:doi:10.1002/ 2014JB011708
- 920 Pearce, M.A., Wheeler, J. & Prior, D.J. (2011) Relative strength of mafic and felsic rocks
921 during amphibolite facies metamorphism and deformation. *J. Struct. Geol.*, **33**, 662–
922 675, Elsevier Ltd. doi:10.1016/j.jsg.2011.01.002
- 923 Pennacchioni, G. & Mancktelow, N.S. (2018) Small-scale ductile shear zones: Neither
924 extending, nor thickening, nor narrowing. *Earth-Science Rev.*, **184**, 1–12.
925 doi:10.1016/j.earscirev.2018.06.004
- 926 Platt, J.P. & Behr, W.M. (2011) Grainsize evolution in ductile shear zones: Implications for
927 strain localization and the strength of the lithosphere. *J. Struct. Geol.*, **33**, 537–550,
928 Elsevier Ltd. doi:10.1016/j.jsg.2011.01.018
- 929 Poirier, J.P. (1985) *Creep of Crystals*, Cambridge University Press.
930 doi:https://doi.org/10.1017/CBO9780511564451
- 931 Powell, R. (1985) Regression diagnostics and robust regression in

- 932 geothermometer/geobarometer calibration: the garnet- clinopyroxene
933 geothermometer revisited. *J. Metamorph. Geol.*, **3**, 231–243.
934 doi:<https://doi.org/10.1111/j.1525-1314.1985.tb00319.x>
- 935 Roberts, D. & Sturt, B.A. (1980) Caledonian deformation in Norway. *J. Geol. Soc. London.*,
936 **137**, 241–250. doi:10.1144/gsjgs.137.3.0241
- 937 Robin, P.Y.F. (1979) Theory of metamorphic segregation and related processes. *Geochim.*
938 *Cosmochim. Acta*, **43**, 1587–1600. doi:10.1016/0016-7037(79)90179-0
- 939 Roermund, H.L.M. van & Lardeaux, J.M. (1991) Modification of antiphase domain sizes in
940 omphacite by dislocation glide and creep mechanisms and its petrological
941 consequences. *Mineral. Mag.*, **55**, 397–407. doi:10.1180/minmag.1991.055.380.09
- 942 Rooney, T.P., Riecker, R.E. & Gavasci, A.T. (1975) Hornblende deformation features. *Geology*,
943 **3**, 364–366.
- 944 Rooney, T.P., Riecker, R.E. & Ross, M. (1970) Deformation Twins in Hornblende. *Science (80-*
945 *).*, **169**, 173–175. doi:10.1126/science.169.3941.173
- 946 Rudnick, R.L. & Fountain, D.M. (1995) Nature and composition of the continental crust: a
947 lower crustal perspective. *Rev. Geophys.*, **33**, 267–309. doi:10.1029/95rg01302
- 948 Rutter, E.H. (1983) Pressure solution in nature, theory and experiment. *J. Geol. Soc. London.*,
949 **140**, 725–740. doi:10.1144/gsjgs.140.5.0725
- 950 Rutter, E.H. & Brodie, K.H. (1985) The permeation of water into hydrating shear zones. in
951 *Metamorphic Reactions: Kinetics, Textures, and Deformation*, pp. 242–250, Springer,
952 New York, NY. doi:10.1007/978-1-4612-5066-1_9

- 953 Rybacki, E. & Dresen, G. (2004) Deformation mechanism maps for feldspar rocks.
954 *Tectonophysics*, **382**, 173–187. doi:10.1016/j.tecto.2004.01.006
- 955 Shannon, R.D. & Rossi, R.C. (1964) Definition of Topotaxy. *Nature*, **202**, 1001–1003.
956 doi:10.1038/2021001a0
- 957 Siegesmund, S., Helming, K. & Kruse, R. (1994) Complete texture analysis of a deformed
958 amphibolite: comparison between neutron diffraction and U-stage data. *J. Struct. Geol.*,
959 **16**, 131–142. doi:10.1016/0191-8141(94)90024-8
- 960 Skemer, P., Katayama, I., Jiang, Z., & Karato, S. I. (2005) The misorientation index:
961 Development of a new method for calculating the strength of lattice-preferred
962 orientation. *Tectonophysics*, **411**(1-4), 157-167. doi:10.1016/j.tecto.2005.08.023
- 963 Skrotzki, W. (1992) Defect structure and deformation mechanisms in naturally deformed
964 hornblende. *Phys. Status Solidi*, **131**, 605–624. doi:10.1002/pssa.2211310232
- 965 Soret, M., Agard, P., Ildefonse, B., Dubacq, B., Prigent, C. & Rosenberg, C. (2019)
966 Deformation mechanisms in mafic amphibolites and granulites: record from the Semail
967 metamorphic sole during subduction infancy. *Solid Earth Discuss.*, 1–36. doi:10.5194/se-
968 2019-28
- 969 Stünitz, H., Fitz Gerald, J.D. & Tullis, J. (2003) Dislocation generation, slip systems, and
970 dynamic recrystallization in experimentally deformed plagioclase single crystals.
971 *Tectonophysics*, **372**, 215–233. doi:10.1016/S0040-1951(03)00241-5
- 972 Stünitz, H. (1993) Transition from fracturing to viscous flow in a naturally deformed
973 metagabbro. in *Defects and processes in the solid state: geoscience applications-the*
974 *MacLaren volume*, pp. 121–150.

- 975 Stünitz, H. (1998) Syndeformational recrystallization - dynamic or compositionally induced?
976 *Contrib. to Mineral. Petrol.*, **131**, 219–236.
- 977 Stünitz, H. & Fitz Gerald, J.D. (1993) Deformation of granitoids at low metamorphic grade. II:
978 Granular flow in albite-rich mylonites. *Tectonophysics*, **221**, 299–324.
979 doi:10.1016/0040-1951(93)90164-F
- 980 Stünitz, H., Neufeld, K., Heilbronner, R., Finstad, A.K., Konopásek, J. & Mackenzie, J.R. (2020)
981 Transformation weakening: Diffusion creep in eclogites as a result of interaction of
982 mineral reactions and deformation. *J. Struct. Geol.*, **139**. doi:10.1016/j.jsg.2020.104129
- 983 Tatham, D.J., Lloyd, G.E., Butler, R.W.H. & Casey, M. (2008) Amphibole and lower crustal
984 seismic properties. *Earth Planet. Sci. Lett.*, **267**, 118–128.
985 doi:10.1016/j.epsl.2007.11.042
- 986 Terry, M.P. & Heidelbach, F. (2006) Deformation-enhanced metamorphic reactions and the
987 rheology of high-pressure shear zones, Western Gneiss Region, Norway. *J. Metamorph.*
988 *Geol.*, **24**, 3–18. doi:10.1111/j.1525-1314.2005.00618.x
- 989 Tullis, J. (1983) Deformation of feldspars. in *Feldspar mineralogy*, pp. 297–323.
- 990 Tullis, J. & Yund, R.A. (1992) The Brittle-Ductile Transition in Feldspar Aggregates: An
991 Experimental Study. *Int. Geophys.*, **51**, 89–117. doi:10.1016/S0074-6142(08)62816-8
- 992 Wheeler, J. (1992) Importance of pressure solution and coble creep in the deformation of
993 polymineralic rocks. *J. Geophys. Res. Solid Earth*, **97**, 4579–4586.
994 doi:10.1029/91JB02476
- 995 White, R.W., Powell, R., Holland, T., Johnson, T.E. & Green, E.C.R. (2014) New mineral
996 activity-composition relations for thermodynamic calculations in metapelitic systems. *J.*

- 997 *Metamorph. Geol.*, **32**, 261–286. doi:10.1111/jmg.12071
- 998 Whitney, D.L. & Evans, B.W. (2010) Abbreviations for names of rock-forming minerals. *Am.*
999 *Mineral.*, **95**, 185–187. doi:10.2138/am.2010.3371
- 1000 Whyte, A.J., Weller, O.M., Copley, A.C. & St-Onge, M.R. (2021) Quantifying Water Diffusivity
1001 and Metamorphic Reaction Rates Within Mountain Belts, and Their Implications for the
1002 Rheology of Cratons. *Geochemistry, Geophys. Geosystems*, **22**, 1–24.
1003 doi:10.1029/2021gc009988
- 1004

Journal Pre-proof

1005 **Tables**

1006 **Table 1: Summary of strain domains present in each thin section. Dominant strain domain present in EBSD maps is shown**
 1007 **below the relevant host thin section.**

Thin Section <i>EBSD map</i>	Strain domain present		
	Low	Mid	High
A8B1	Y		
<i>1a</i>	Y		
<i>1b</i>	Y		
A8B2	Y		
<i>2a</i>	Y		
<i>2b</i>	Y		
A8B3	Y	Y	Y
<i>3a</i>	Y		
<i>3b</i>			Y
<i>3c</i>		Y	
<i>3d</i>			Y
A8B4	Y	Y	Y
<i>4a</i>		Y	
<i>4b</i>		Y	
<i>4c</i>			Y
A8B5		Y	Y
<i>5a</i>		Y	
<i>5b</i>		Y	
A8B6	Y	Y	Y
<i>6a</i>		Y	
A8B7			Y
<i>7a</i>			Y
<i>7b</i>			Y
A8B8			Y
<i>8a</i>			Y
A8B9			Y
<i>9a</i>			Y
<i>9b</i>			Y
A8B10	Y		
<i>10a</i>	Y		
<i>10b</i>	Y		

1008

Table 2: Selected representative analyses of garnet, clinopyroxene, plagioclase and amphibole from point analysis.

Min. Thin section	Grt A8b4	Grt A8b4	Grt A8b9	Cpx A8b1	Cpx A8b1	Cpx A8b4	Cpx A8b4	Pl A8b1	Pl A8b1	Pl A8b4	Pl A8b9	Pl A8b9	Amp A8b1	Amp A8b4	Amp A8b4	Amp A8b9
Anal.	256/1	111/1	125/6	15/1	87/1	224/1	92/1	101/8	61/1	212/1	44/1	12/1	60/1	211/1	364/1	119/1
SiO ₂	38.15	38.33	38.18	53.94	53.22	53.77	52.45	54.46	58.2	59.24	59.9	62.12	42.1	43.79	52.47	43.34
TiO ₂	0.06	0.01	0.06	0.11	0.13	0.10	0.06	0.00	0.00	0.00	0.00	0.00	1.23	1.48	0.34	1.18
Al ₂ O ₃	21.24	20.82	21.06	1.12	1.39	1.18	1.06	29.55	27.36	25.88	25.30	23.83	16.47	13.53	5.48	12.77
FeO	25.01	24.31	25.22	7.13	8.64	6.78	11.22	0.00	0.00	0.00	0.00	0.00	12.85	13.20	9.45	15.37
MnO	1.50	0.95	2.34	0.14	0.25	0.12	0.06	0.00	0.00	0.00	0.00	0.00	0.20	0.04	0.14	0.19
MgO	4.70	2.76	3.50	13.87	13.12	13.95	12.07	0.00	0.00	0.00	0.00	0.00	10.00	11.05	16.49	10.37
CaO	9.28	13.37	9.78	23.39	23.08	23.81	22.37	11.33	8.76	7.68	7.03	5.24	11.49	11.59	11.80	11.07
Na ₂ O	0.02	0.01	0.00	0.51	0.52	0.57	0.62	5.07	6.50	7.36	7.47	8.51	2.26	2.13	0.81	1.91
K ₂ O	0.00	0.00	0.04	0.00	0.00	0.00	0.00	0.00	0.05	0.07	0.09	0.06	0.46	0.43	0.09	0.46
Σ	100.0	100.5	100.2	100.2	100.4	100.3	99.9	100.4	100.8	100.2	100.0	99.8	97.1	97.2	97.1	96.7
Ox.	12	12	12	6	6	6	6	8	8	8	8	8	23	23	23	23
Si	2.99	3.01	3.01	1.99	1.98	1.99	1.98	2.44	2.58	2.64	2.67	2.75	6.20	6.44	7.43	6.42
Ti	0.00	0.00	0.00	0.00	0.00	0.00	0.00	0.00	0.00	0.00	0.00	0.00	2.86	2.35	0.91	2.23
Al	1.96	1.92	1.95	0.05	0.06	0.05	0.05	1.56	1.42	1.36	1.33	1.25	0.14	0.16	0.04	0.13
Fe _{tot}	1.64	1.59	1.66	0.22	0.27	0.21	0.35	0.00	0.00	0.00	0.00	0.00	1.58	1.62	1.12	1.90
Mn	0.10	0.06	0.16	0.00	0.01	0.00	0.00	0.00	0.00	0.00	0.00	0.00	0.02	0.01	0.02	0.02
Mg	0.55	0.32	0.41	0.76	0.73	0.77	0.68	0.00	0.00	0.00	0.00	0.00	2.20	2.42	3.48	2.29
Ca	0.78	1.12	0.82	0.93	0.92	0.94	0.91	0.55	0.42	0.37	0.36	0.25	1.81	1.83	1.79	1.76
Na	0.00	0.00	0.00	0.04	0.04	0.04	0.05	0.44	0.56	0.63	0.64	0.73	0.65	0.61	0.22	0.55
K	0.00	0.00	0.00	0.00	0.00	0.00	0.00	0.00	0.00	0.00	0.00	0.00	0.09	0.08	0.02	0.09
Prp	0.18	0.10	0.13	-	-	-	-	-	-	-	-	-	-	-	-	-
Alm	0.53	0.51	0.54	-	-	-	-	-	-	-	-	-	-	-	-	-
Grs	0.25	0.36	0.27	-	-	-	-	-	-	-	-	-	-	-	-	-
Sps	0.03	0.02	0.05	-	-	-	-	-	-	-	-	-	-	-	-	-
Mg#	0.25	0.17	0.20	0.78	0.73	0.79	0.66	-	-	-	-	-	0.58	0.60	0.76	0.55
An#	-	-	-	-	-	-	-	0.56	0.43	0.37	0.36	0.26	-	-	-	-

Abbreviations after Whitney and Evans (2010).

1009

1010

1011

1012 **Figure captions**

1013 Figure 1: Geological map of the study area in Northern Norway. (a) North Norwegian
 1014 Caledonides focussing on the Tromsø to Kalak Nappe Complexes. (b) Detailed map of Arnøya
 1015 and Kågen to highlight the sample area in the Kågen gabbro. (c) Cross section through Arnøya
 1016 and Kågen showing the gabbro intruded into the Vaddas Nappe. The density of red lines
 1017 corresponds to the intensity of ductile deformation within and along boundaries between
 1018 individual nappes. Caledonian foliations are shown in red, whereas black ones are possibly
 1019 pre-date Caledonian deformation. After Faber et al. (2019).

1020

1021 Figure 2: (a) Outcrop photograph of sample area (GPS: 70.04387°N, 20.71438°E), boundaries
 1022 between low and high deformation areas highlighted by yellow dashed lines. (b) Detailed
 1023 photograph from (a) with deformation boundaries and low/high strain zones identified. (c)
 1024 Photograph of sample A8B with thin section locations highlighted by orange boxes,
 1025 deformation boundaries between low, mid and high strain zones identified. LS, low strain; MS,
 1026 mid strain; HS, high strain.

1027

1028 Figure 3: Overview thin section photomicrographs of representative (a) low, (b) mid and (c)
 1029 high strain areas in sample A8B. (a) The low strain area shows clinopyroxene grains
 1030 surrounded by amphibole coronas. Areas of chemical analysis (Fig. 7a) and EBSD (Fig. 9a) are
 1031 indicated. (b) A characteristic mid strain area bound to the top by a low strain zone, and below
 1032 by a high strain domain. Amphibole replacement of clinopyroxene is more extensive and
 1033 plagioclase is highly recrystallized. Box Fig. 9b indicates area of EBSD analysis. (c) High strain
 1034 region with amphibole and plagioclase layers. Garnet profile for Fig. 6f and EBSD map area for
 1035 Fig. 9c are indicated.

1036

1037 Figure 4: Detailed thin section photomicrographs of specific textures in (a-c) low, (d-f) mid and
 1038 (g-i) high strain areas in sample A8B. Low strain: (a-b) clinopyroxene grain with recrystallized
 1039 fracture and amphibole rim; (c) zoisite and isolated amphibole grains with pl_1 and pl_2
 1040 plagioclase grains. Mid strain: (d) cpx1 grain with garnet rim, rim reaction is amphibole poor;
 1041 (e) clinopyroxene grain with garnet rim on the top and amphibole rim below; (f) amphibole
 1042 replacement of clinopyroxene, top section between arrows shows complete amphibole
 1043 replacement, below this original clinopyroxene grains are still preserved. High strain: (g)
 1044 garnet within amphibole zone; (h-i) amphibole-plagioclase layers, amphibole is olive green
 1045 coloured when associated with ilmenite (amp_{B1}) and otherwise jade green coloured (amp_{B2}).
 1046 All photomicrographs are in plane polarised light except (b) that is under cross-polarised light.

1047

1048 Figure 5: Grain size and shape properties for amphibole and plagioclase grains. (a-c) Grain size
 1049 distribution with grain statistics for amphibole and plagioclase grains in low to high strain
 1050 areas of the sample. (d-f) Normalised grain orientation or shape preferred orientation of
 1051 amphibole and plagioclase grains in low to high strain areas. Grain data for each strain area is

1052 grouped together, low strain data includes data from EBSD maps 1a, 1b, 2a, 2b, 3a, 10a and
 1053 10b; mid strain data includes EBSD maps from 3c, 4b, 4c, 5a, 5b and 6a; and high strain data
 1054 includes EBSD maps from 3b, 3d, 4a, 7a, 7b, 8a, 9a and 9b. Number of grains considered for
 1055 each strain area is indicated by n_g . The frequency for rose diagrams is 0-1 and grain orientation
 1056 is in the kinematic reference frame (the same as CPO pole figures in Figures 9-11).

1057

1058 Figure 6: BSE images and compositional maps of detailed microstructural features in (a) low,
 1059 (b-c) mid and (d) high strain areas of the Kågen gabbro margins. (a) Edge of clinopyroxene
 1060 grain from Figure 3a, Mg and Na chemical maps highlight variations in clinopyroxene,
 1061 amphibole and plagioclase chemistry. New small grains surrounding or forming tails around
 1062 magmatic porphyroclasts have lower Mg and higher Na value than the original clinopyroxene
 1063 grain (b) Clinopyroxene grain with amphibole replacement and garnet band, Mg and Na maps
 1064 highlight variations in clinopyroxene and amphibole chemistry associated neighbour grains.
 1065 (c) Amphibole-poor clinopyroxene grain from Figure 4d. Mg map highlights the variation in
 1066 garnet chemistry when adjacent to plagioclase (low) or clinopyroxene/ilmenite (high).
 1067 Plagioclase shows elevated Na when adjacent to garnet or amphibole as opposed to the core
 1068 of pl_1 grains. New pl_2 grains are also have a higher Na. (d) Amphibole band in a high strain
 1069 region. Mg- and Si-rich cores in amp_{B1} (olive green coloured) compared to amp_{B2} (jade green
 1070 coloured).

1071

1072 Figure 7: Point analyses and compositions for (a) clinopyroxene, (b-c) amphibole, (d)
 1073 plagioclase and (e-f) garnet from low (A8B1), mid (A8B4) and high (A8B9) high strain areas of
 1074 the Kågen gabbro margins.

1075

1076 Figure 8: Estimated P-T conditions for the high strain areas of the Kågen gabbro margins.
 1077 Isopleths represent end-member garnet and anorthite compositions. P-T conditions for high
 1078 strain areas of the sample are in the highlighted box, observed and calculate compositions for
 1079 garnet end-members (Alm, Grs, Prp), anorthite content (An) and amphibole (Amp) are shown
 1080 in the bottom right. Oxide totals for pseudosection calculation are from a XRF measurements
 1081 of a high strain area: Na_2O 2.88, MgO 8.27, Al_2O_3 14.11, SiO_2 49.97, CaO 11.49, FeO 8.54, H_2O
 1082 1.15. Inset shows amphibole-plagioclase thermobarometry for low, mid and high strain areas.

1083

1084 Figure 9: (a) EBSD maps of amphibole orientations coloured parallel to the X direction, all other
 1085 minerals are shown in grey. All maps are at the same scale to highlight the change in grain size
 1086 and texture between the differently deformed areas. (b) Pole figures showing amphibole CPO
 1087 for the low to high strain areas, and clinopyroxene CPO for the low and mid strain areas.
 1088 Clinopyroxene CPO's are not plotted for the high strain area as there is less than 1% present
 1089 in the map giving skewed results due to lack of grains. All pole figures are equal area, lower
 1090 hemisphere projections plotted as point per grain. J-index, M-index and number of grains (n_g)
 1091 is shown for each set of pole figures. (c) Distribution of misorientation angles between
 1092 correlated (adjacent) pixels (histogram) and between uncorrelated pixels (orange curve) of
 1093 amphibole. The uniform (green) curve corresponds to the theoretical misorientation

1094 distribution for perfectly randomly oriented crystals. (d) Amphibole and clinopyroxene inverse
1095 pole figures showing the distribution of correlated misorientation axes (between 2 and 10°).
1096 All contours are multiples of uniform distribution (m.u.d).

1097

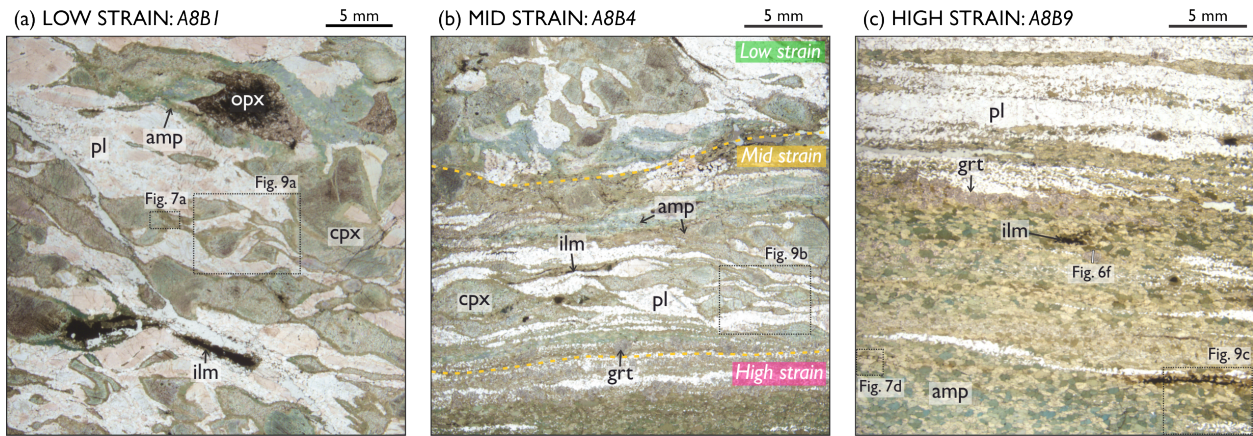
1098 Figure 10: EBSD phase map of a clinopyroxene grain with amphibole corona, below are CPO
1099 pole figures for selected regions associated with the clinopyroxene grain. Region A (red)
1100 includes the clinopyroxene and all grains that mantle it. Region B (blue) contains the
1101 recrystallized portion of the clinopyroxene grain and the amphibole grains that mantle and
1102 are included in the clinopyroxene grain. Region C (orange) focusses on the right hand side of
1103 the clinopyroxene grain and the amphibole inclusions within the grain. Region D (purple)
1104 includes the clinopyroxene and amphibole grains in the recrystallized tail. All pole figures are
1105 equal area, lower hemisphere projections plotted as point per grain.

1106

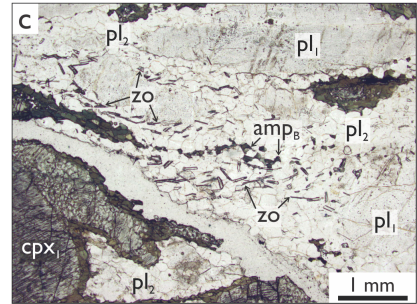
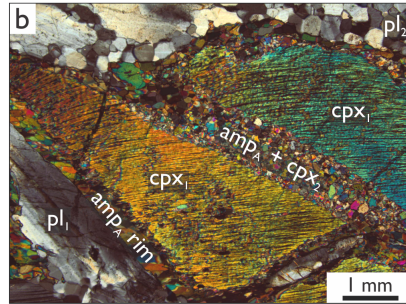
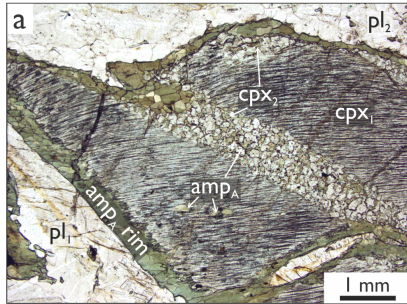
1107 Figure 11: EBSD map and plagioclase CPO pole figures for representative (a) low, (b) mid and
1108 (c) high strain areas. EBSD maps show plagioclase orientations coloured parallel to the X
1109 direction, all other minerals are shown in grey. Pole figures showing plagioclase CPO, for (c),
1110 additional CPO are included for polyphase and monophase areas as well as the amphibole
1111 whole map CPO is also included (amphibole CPO for a and b are shown in Figure 9). All pole
1112 figures are equal area, lower hemisphere projections plotted as point per grain. J-index, M-
1113 index and number of grains (n_g) is shown for each set of pole figures.

1114

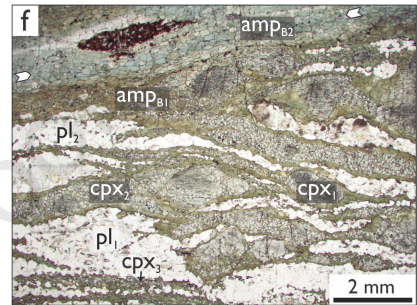
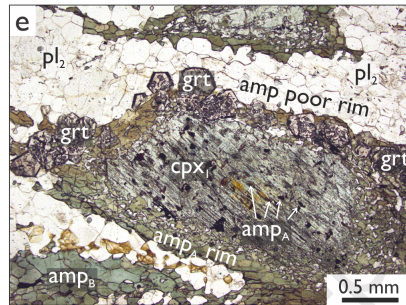
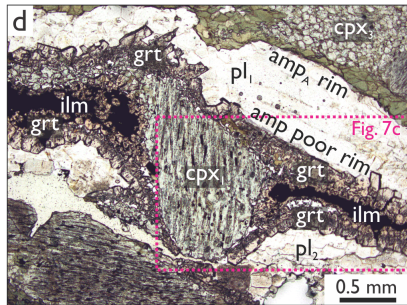
1115 Figure 12: (a) Composite P-T-t evolution of Kågen gabbro and Vaddas Nappe utilising P-T
1116 estimates from this study for the hydration-deformation event, Getsinger et al. (2013) for the
1117 Kågen gabbro intrusion and Faber et al. (2019) for Vaddas Nappe metasediments and Kalak-
1118 Vaddas boundary. (b) Schematic diagram of the microstructural evolution of Kågen gabbro
1119 margins when deformation occurred under differing hydration conditions. The low strain
1120 example represents 'dry' conditions where the amphibole CPO is host-controlled and
1121 inherited from clinopyroxene. The high strain example represents fluid saturated conditions
1122 where the amphibole CPO is controlled by orientated growth.



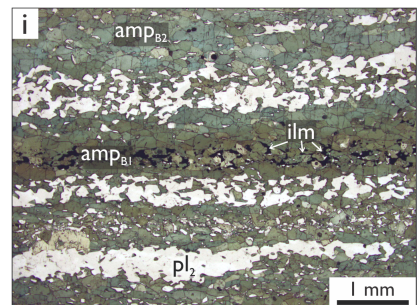
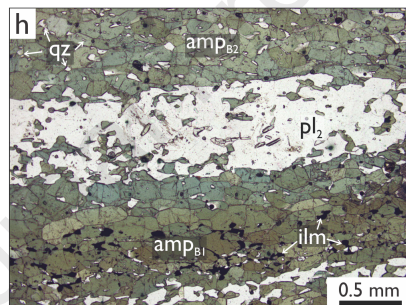
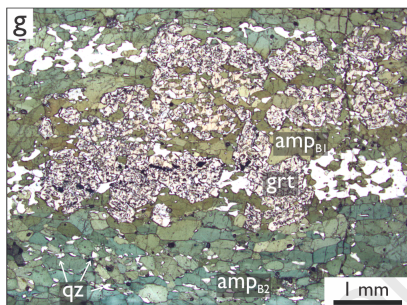
LOW STRAIN: A8B1

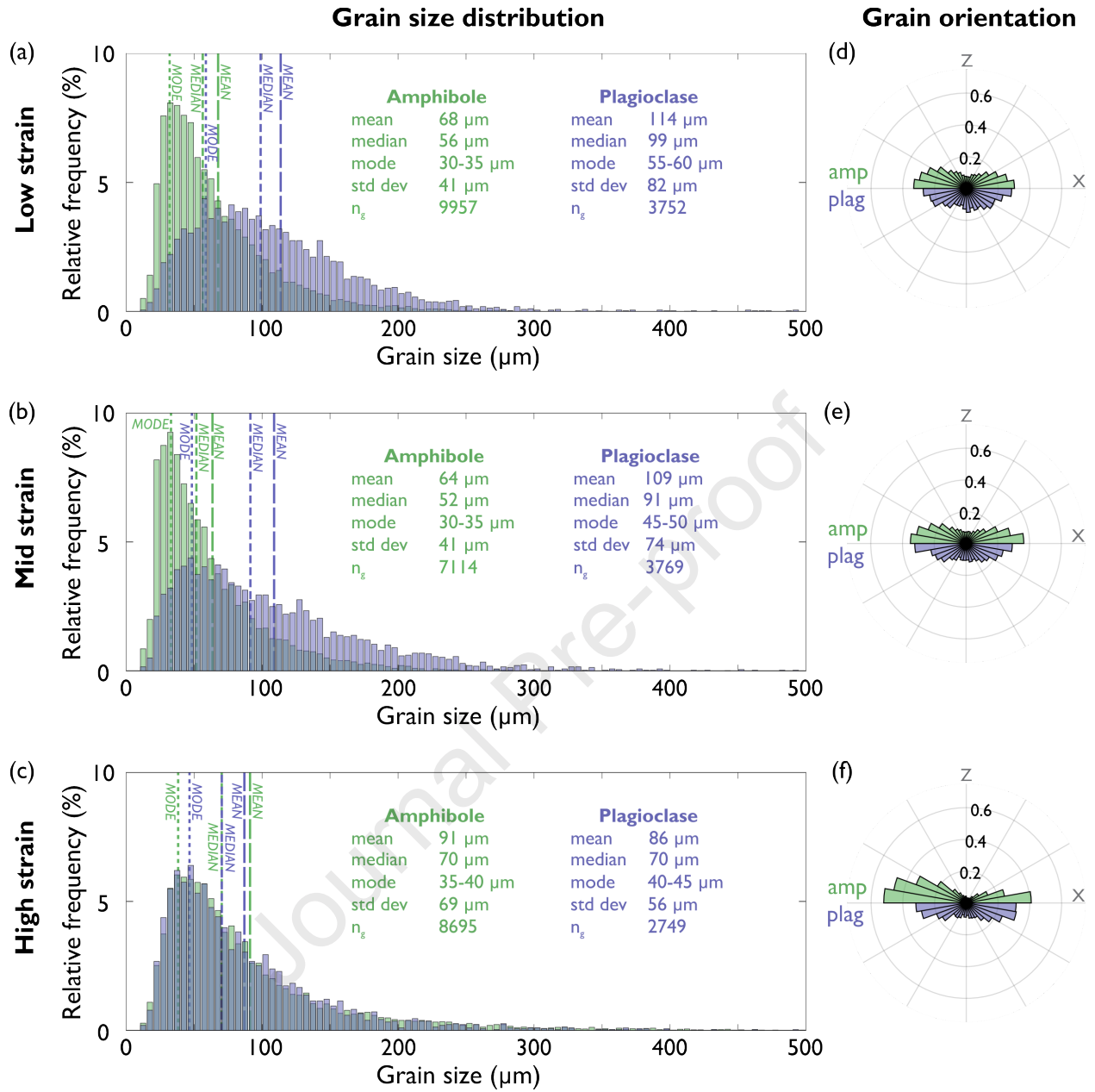


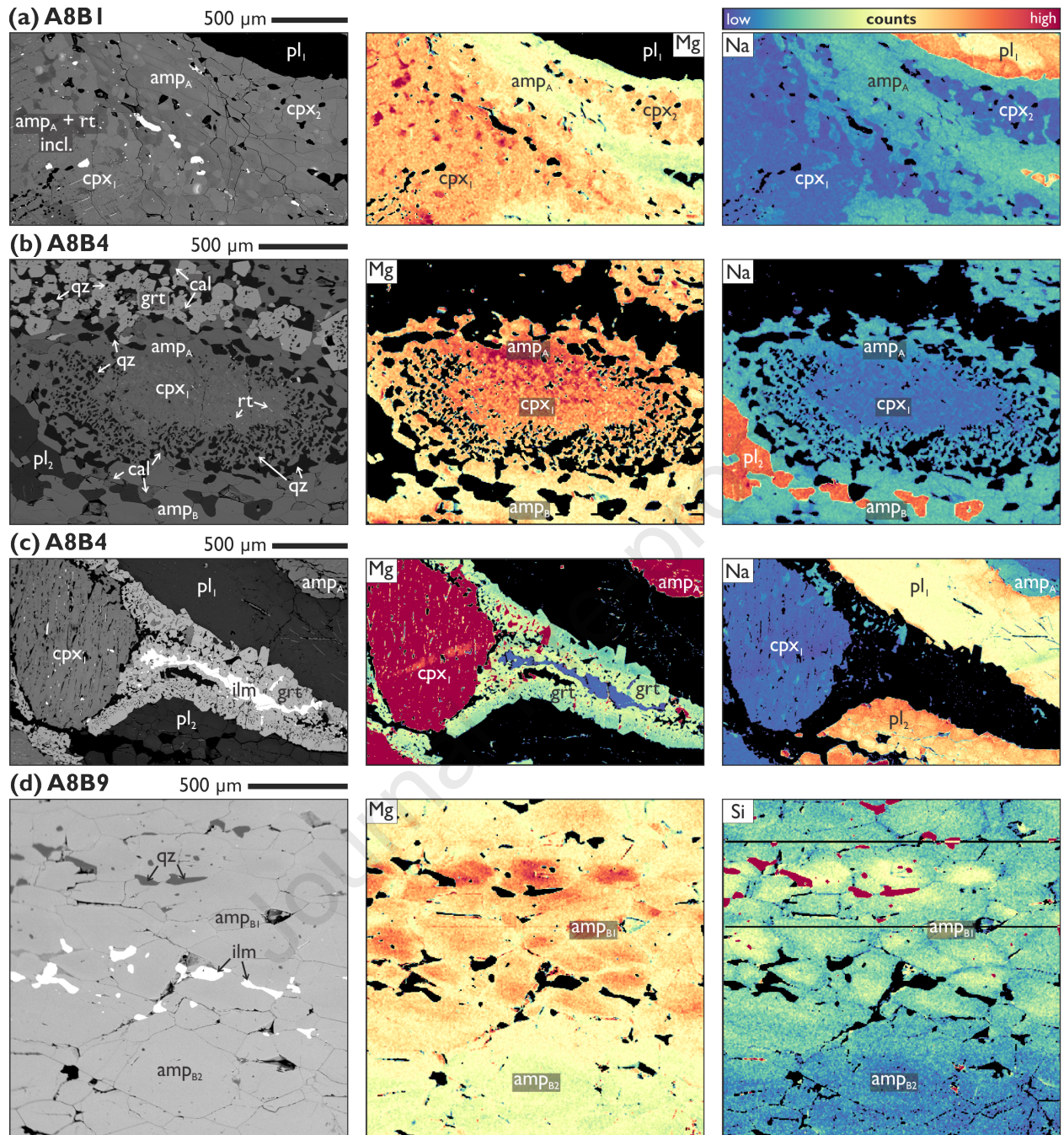
MID STRAIN: A8B4

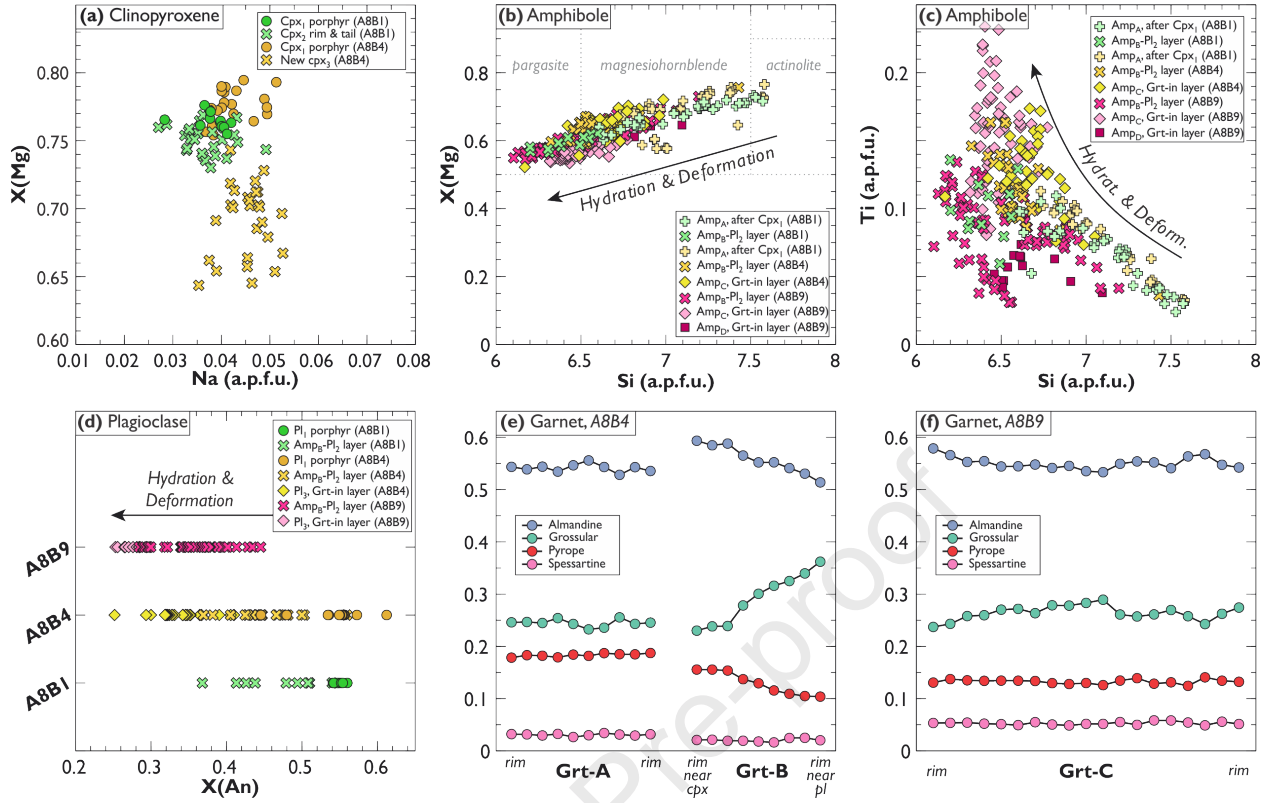


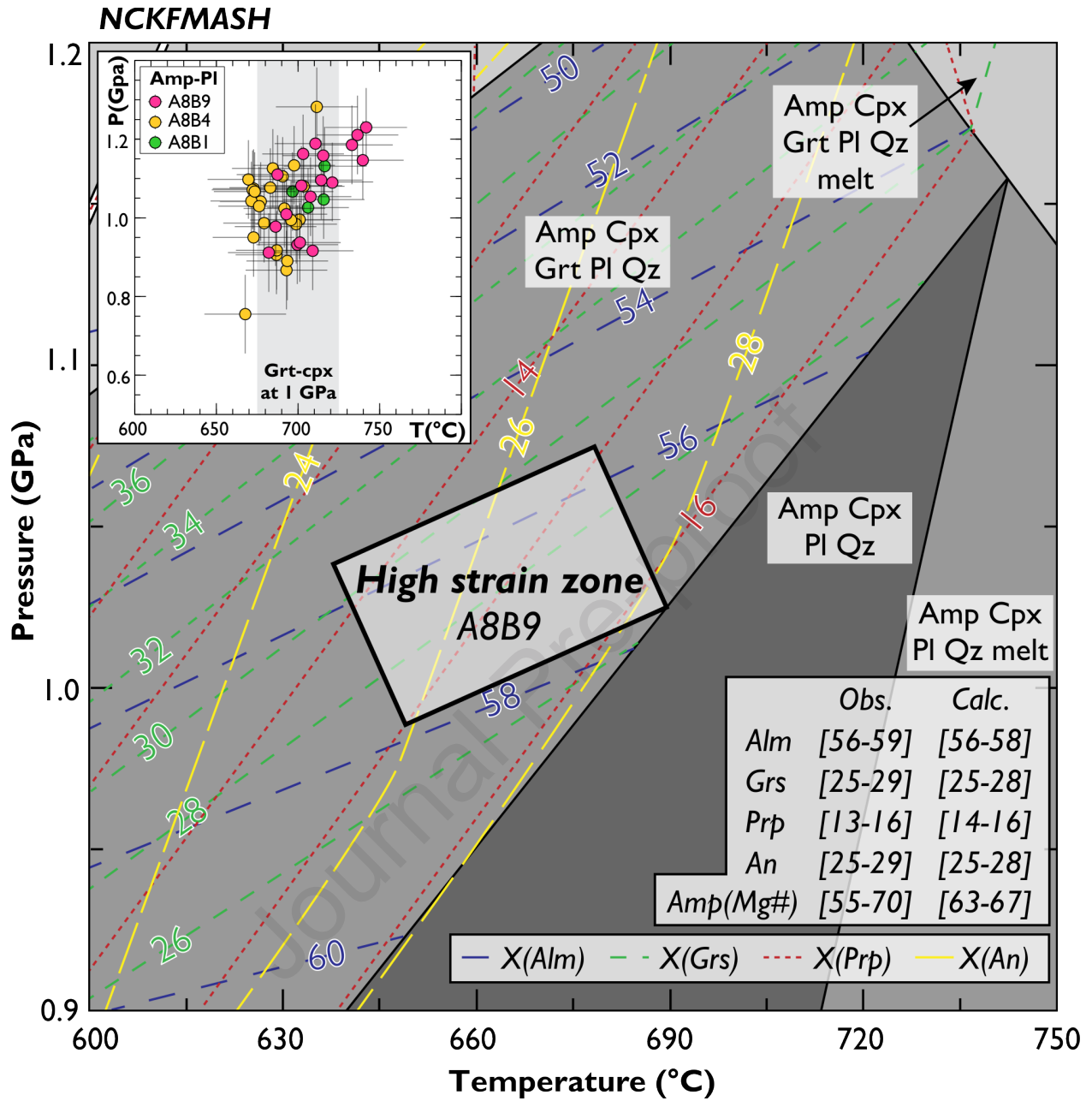
HIGH STRAIN: A8B7



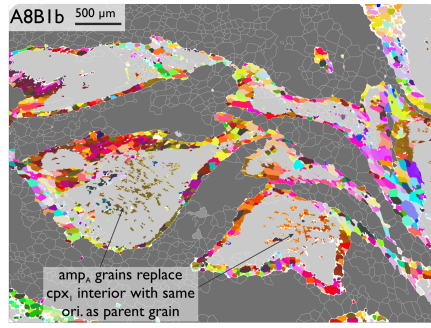




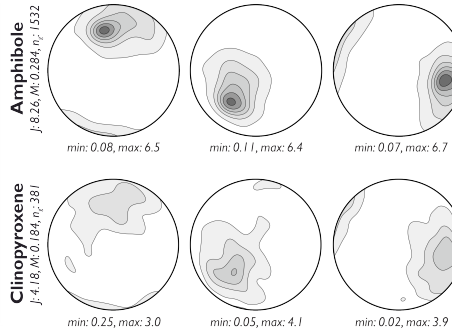




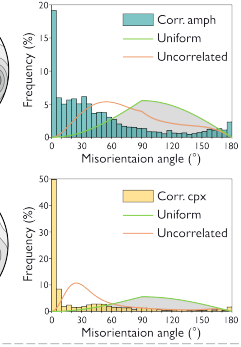
(a) **Low strain:**



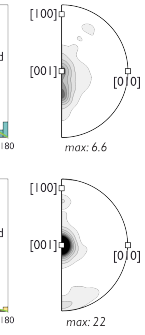
(b) (100) (010) [001]



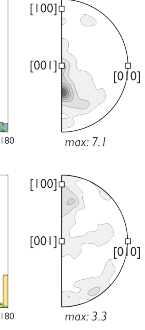
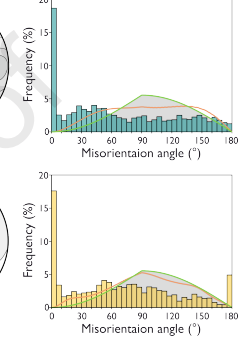
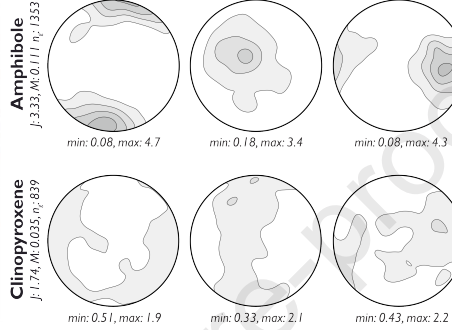
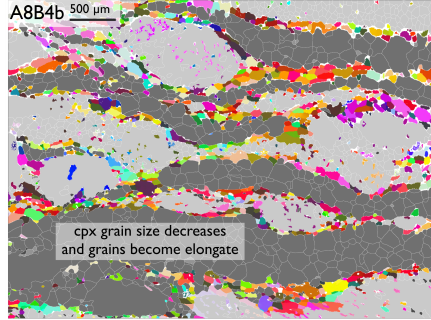
(c)



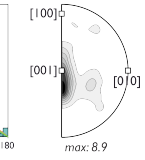
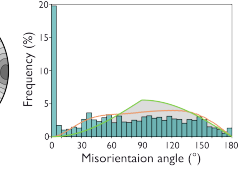
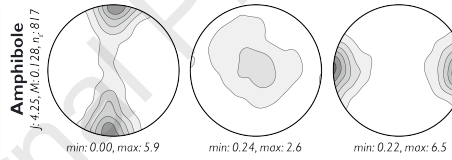
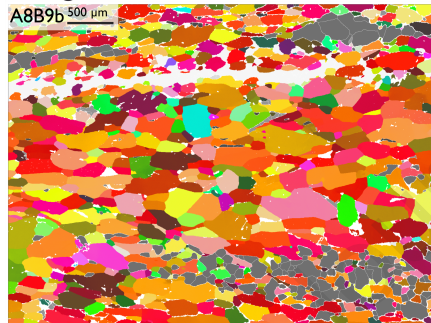
(d) Mis. axes 2-10 $^\circ$



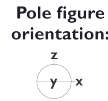
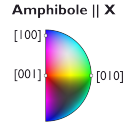
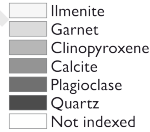
Mid strain:

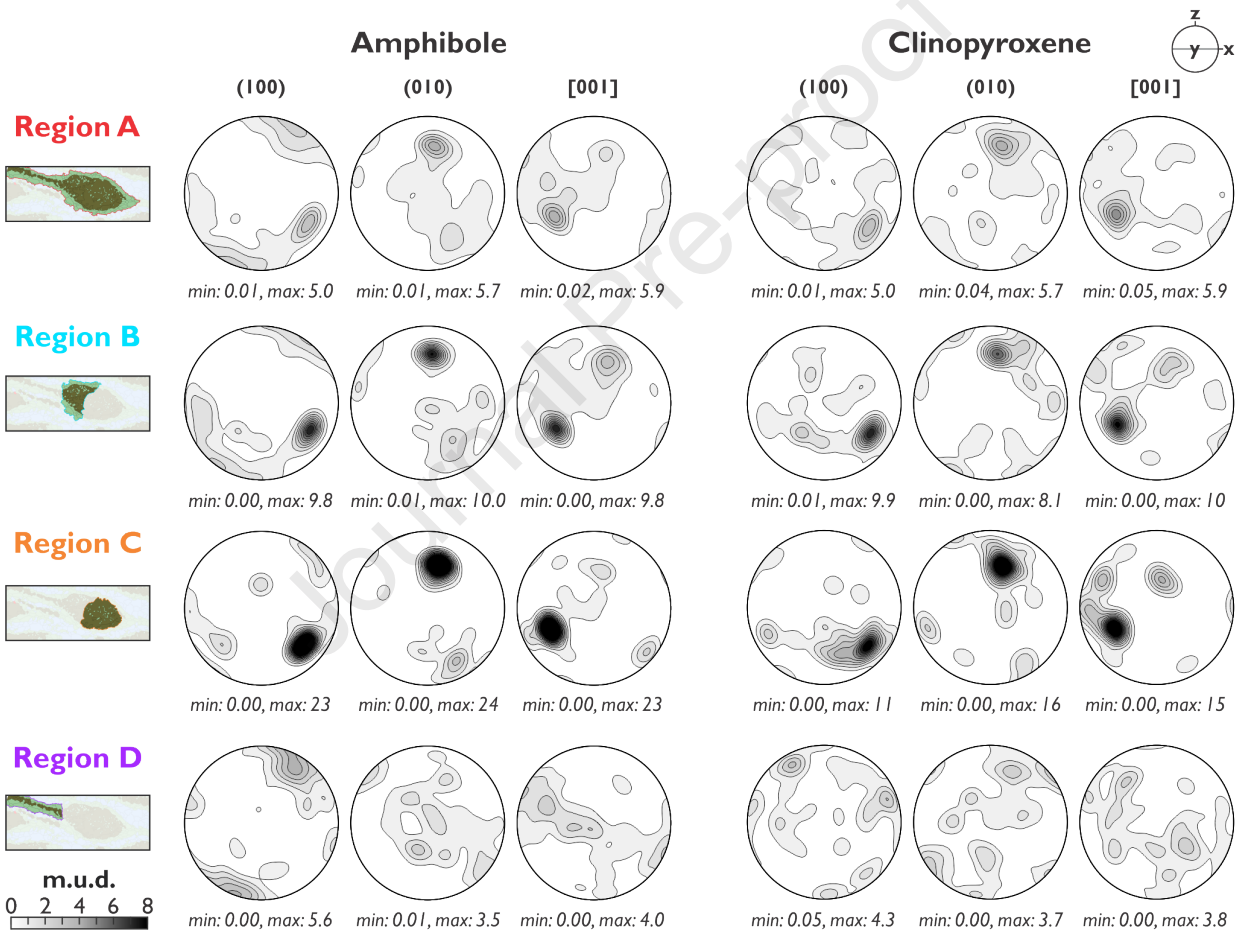
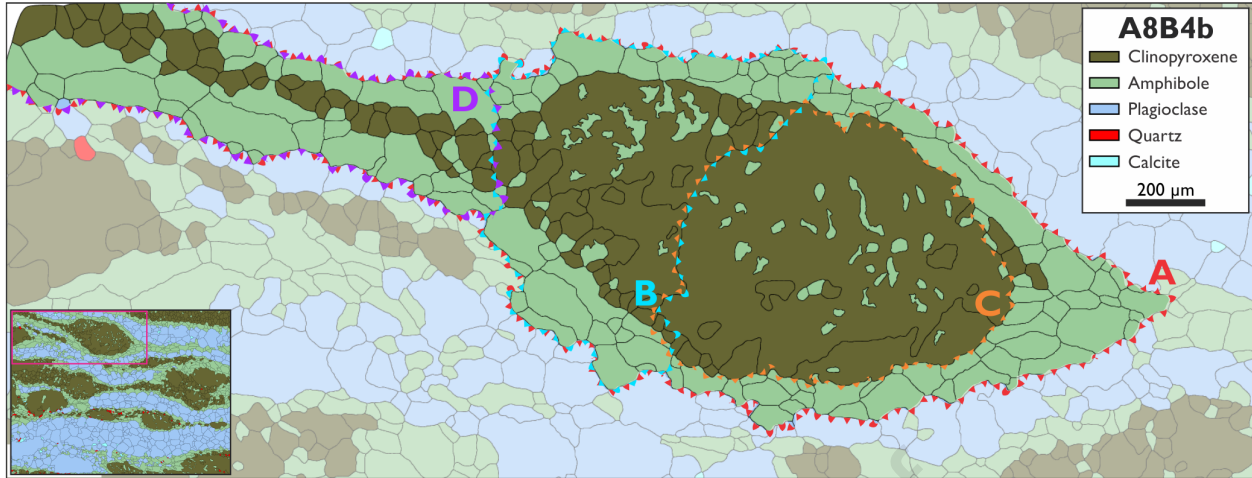


High strain:

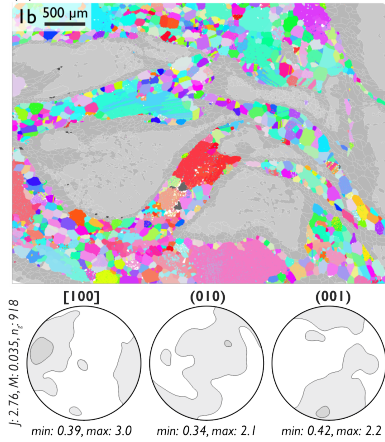


EBSD maps:

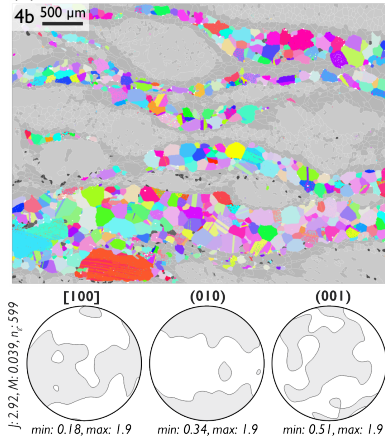




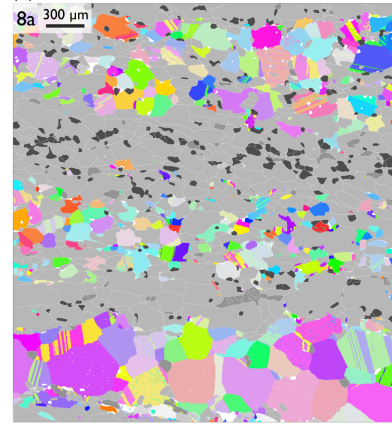
(a) **LOW STRAIN**



(b) **MID STRAIN**

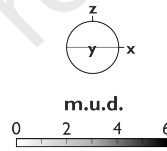
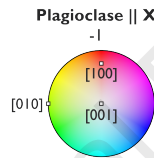


(c) **HIGH STRAIN**

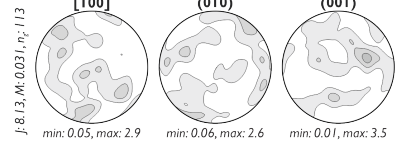


EBSD maps:

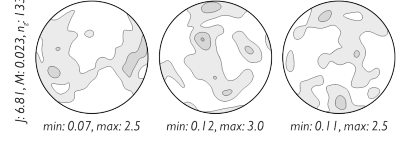
- Ilmenite
- Garnet
- Clinopyroxene
- Amphibole
- Calcite
- Quartz
- Not indexed



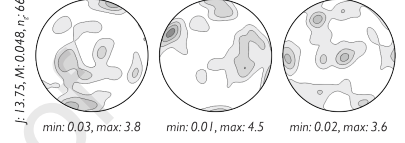
PLAGIOCLASE IN PARTLY POLYPHASE LAYER



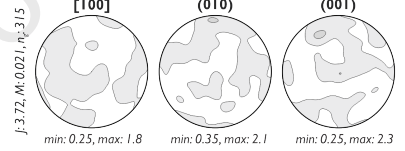
PLAGIOCLASE IN POLYPHASE LAYER



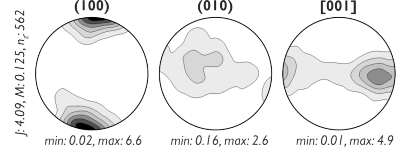
MONOPHASE PLAGIOCLASE LAYER

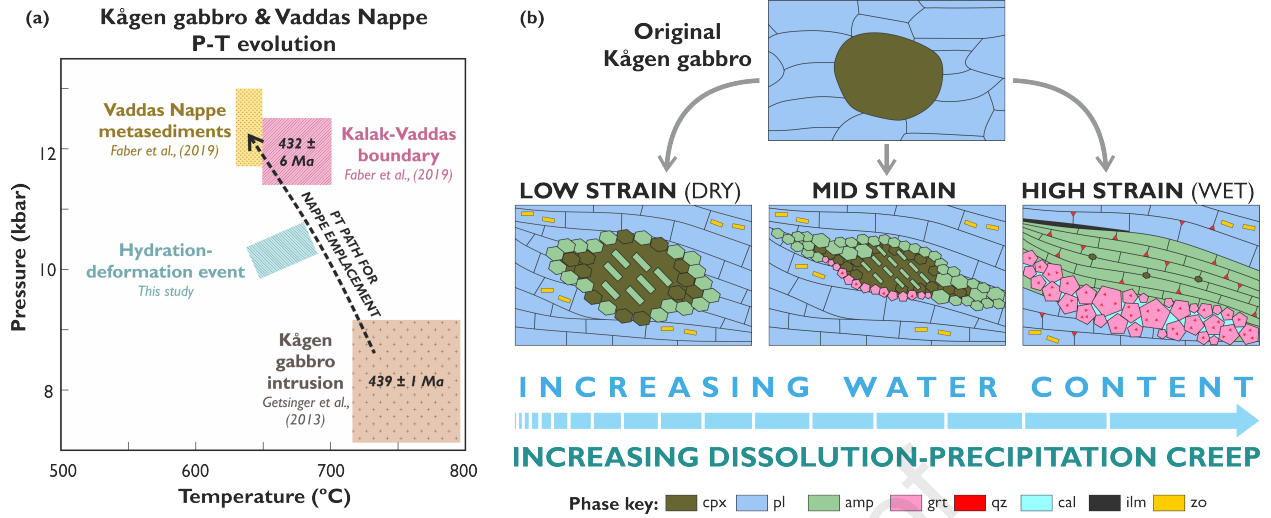


PLAGIOCLASE FOR WHOLE HIGH STRAIN MAP



AMPHIBOLE FOR WHOLE HIGH STRAIN MAP





Highlights

1. Deformation and coupled mineral reactions mechanically weaken strong mafic rocks.
2. Dissol.-precip.-creep allows viscous deformation of mafics at low temperatures.
3. CPO may form by growth mechanisms and shape factors instead of crystal plasticity.

Journal Pre-proof

Declaration of interests

The authors declare that they have no known competing financial interests or personal relationships that could have appeared to influence the work reported in this paper.

The authors declare the following financial interests/personal relationships which may be considered as potential competing interests:

Journal Pre-proof